Chemical Science

ROYAL SOCIETY OF CHEMISTRY

PERSPECTIVE

View Article Online
View Journal

Cite this: DOI: 10.1039/d5sc05663b

All publication charges for this article have been paid for by the Royal Society of Chemistry

Synergistic energy and charge transfer dynamics in LD/3D perovskite heterojunctions for optoelectronic applications

Bidisha Nath, [a] Pradhi Srivastava,[b] Junjie Xie, [a] Tajamul A. Wani,[a] Karima Al-Hawiti,[a] Xiaohan Jia,[a] Neha Arora[c] and M. Ibrahim Dar *[a]

The functionality of low-dimensional (LD)/three-dimensional (3D) heterojunctions is governed by factors such as lattice mismatch, surface potential, and controlled growth conditions, all of which critically influence charge and energy transfer dynamics. By strategically tuning the heterointerface through optimised organic cations and conjugated ligands, efficient charge transfer and reduced recombination losses can be achieved, leading to improved power conversion efficiency for solar cells and luminescence quantum yield for light-emitting devices. This perspective explores the fundamental photophysical processes at the LD/3D interface, including exciton dissociation, charge carrier trapping, and electron–phonon coupling, which play a key role in determining device performance. We discuss the interplay of charge and energy transport mechanisms, focusing on Dexter energy transfer (DET), Förster resonance energy transfer (FRET), and triplet energy transfer (TET), and their impact on minimising non-radiative recombination and optimising charge extraction. Furthermore, we highlight how heterojunction engineering influences quasi-Fermi level splitting, built-in potential formation, and defect passivation, contributing to enhanced stability and long-term operational durability. A comprehensive understanding of these synergistic processes offers new pathways for the design of advanced perovskite-based optoelectronic devices, paving the way for next-generation high-performance photovoltaics and light-emitting applications.

Received 28th July 2025
Accepted 15th April 2026

DOI: 10.1039/d5sc05663b

rsc.li/chemical-science

[a]Cavendish Laboratory, Department of Physics, University of Cambridge, Cambridge CB3 0US, UK. E-mail: id338@cam.ac.uk
[b]Department of Physics, Harish-Chandra Research Institute (HRI) Allahabad, A C.I. of Homi Bhabha National Institute (HBNI), Chhatnag Road Jhunsi, Prayagraj 211019, India
[c]Department of Chemistry, University College London, London, WC1H 0AJ, UK

1. Introduction

Heterojunctions based on LD/3D perovskite layers have emerged as promising architectures to enhance the stability

Bidisha Nath

Bidisha Nath is a Postdoctoral Researcher in the Cavendish Laboratory at the University of Cambridge. She is working on recombination dynamics in halide perovskites. Her research experience also spans interface engineering, perovskite device optimisation and characterisation. She received her PhD degree from Indian Institute of Science, Bangalore, India.

Pradhi Srivastava

Pradhi Srivastava is currently a Postdoctoral Fellow at the Harish Chandra Research Institute, Prayagraj, India. She earned her PhD from the Indian Institute of Science Education and Research (IISER) Bhopal, where she investigated structural phase transitions in over-tolerant hybrid perovskites ($MHyPbX_3$) using first-principles methods. Her current research interests encompass electron–phonon coupling, excited-state dynamics, and spin-splitting effects across a wide range of materials, including perovskites and chalcogenides, aiming to understand and tailor their fundamental optoelectronic and spintronic properties.

and efficiency of optoelectronic devices by integrating the superior charge transport of 3D perovskites with the structural and chemical robustness of LD phases.

LD[1] (including zero-dimensional (0D), one-dimensional (1D),[2] and two-dimensional (2D)), quasi-2D, and three-dimensional (3D) perovskites[3] exhibit distinct optoelectronic properties, which can be synergistically combined in a heterojunction to achieve superior device performance. The structure of perovskite with different dimensionalities, as shown in Fig. 1(a), plays an important role in the charge and energy transport mechanism and efficiency. The fundamental structural unit of metal halide perovskites is the ($[BX]_6^{4-}$) octahedron.[4] 3D perovskites, such as $MAPbI_3$, exhibit a cubic or tetragonal structure with a pseudo-cubic lattice parameter of ~6.3 Å,[5] where BX_6 octahedra (*e.g.*, PbI_6) form a continuous 3D network. In contrast, 2D perovskites, such as Ruddlesden–Popper (RP) phases ($A'_2A_{n-1}B_nX_{3n+1}$), feature a layered structure where inorganic slabs (BX_6 octahedra) are separated by organic spacer

Junjie Xie

Junjie Xie is a PhD student in the Cavendish Laboratory at the University of Cambridge. His research focuses on understanding ion migration dynamics in perovskite semiconductors and solar cells. He completed his Master's degree (MRes) at Imperial College London in 2024.

Tajamul A. Wani

Tajamul A. Wani is part of the EPSRC Centre for Doctoral Training (CDT) in Compound Semiconductor Manufacturing, jointly hosted by Cardiff University, University College London, the University of Manchester, and the University of Sheffield. Tajamul A. Wani has completed his Master of Technology in Materials Engineering at the Indian Institute of Technology Delhi, India. His research interests include III–V compound and emerging semiconductors for optoelectronic applications.

Karima Al-Hawiti is a PhD student in the Cavendish Laboratory at the University of Cambridge. Her research focuses on the nucleation and crystallisation of halide perovskite semiconductors, and she is particularly interested in how low-dimensional systems influence the thermodynamic stability and photophysical properties of 3D perovskite frameworks.

Xiaohan Jia

Xiaohan Jia is currently a PhD student in the Cavendish Laboratory at the University of Cambridge. Her research focuses on understanding and minimising photovoltage deficits in wide-bandgap perovskite solar cells. Before starting her doctoral studies, she worked from 2021 to 2023 as a research assistant in Prof. Rui Zhu's group in the Department of Physics at Peking University. She received her MSci degree in Chemistry from University College London (UCL) in 2021.

Neha Arora

Neha Arora is a Lecturer (Teaching) in Inorganic and Materials Chemistry at UCL. Before this, she was a Research Associate with Prof. Sir Richard Friend at the Cavendish Laboratory in the University of Cambridge (2018–2021), where she focused on next-generation solid-state materials for applications in solar cells and light-emitting devices. From 2016–2018, she worked as a Postdoctoral Scientist with Prof. Michael Grätzel at EPFL, where her research focused on the fabrication and understanding of perovskite solar cells yielding high efficiencies and remarkable photovoltages.

M. Ibrahim Dar

M. Ibrahim Dar is a Royal Society University Research Fellow and a group leader in the Cavendish Laboratory at the University of Cambridge. Prior to this, he was an Advanced Swiss National Science Foundation Post-Doctoral Fellow with Professor Sir Richard Friend, unravelling the photophysics of perovskite devices (2018–2020). He also worked as a Post-Doctoral Scientist with Prof. Michael Grätzel at EPFL, Switzerland (2014–2018), focusing on emerging semiconductors for their application in highly efficient solar cells. His group at Cavendish conducts interdisciplinary research that combines solid-state chemistry, photophysics, and nanoscience to design and understand emerging semiconductors for solar cells and light-emitting applications.

cations (*e.g.* propylammonium (PA^+), butylammonium (BA^+), phenylethylammonium (PEA^+)), creating large interlayer distances with weak van der Waals interactions. While their in-plane lattice parameters are comparable to 3D perovskites, the out-of-plane spacing is significantly larger (depending on the organic cation), introducing structural anisotropy.[6] In contrast, the Dion–Jacobson (DJ) phase ($A'A_{n-1}B_nX_{3n+1}$) contains a single layer of interlayer cations, eliminating van der Waals gaps and strengthening electronic coupling, thereby enhancing charge mobility. The alternating cation interleaved (ACI) phase ($A'A_nB_nX_{3n+1}$) exhibits a compact stacking arrangement, reducing interlayer spacing and promoting out-of-plane charge transport.[7]

In 0D systems,[8] such as quantum dots, strong quantum confinement and tunable emission wavelengths make them attractive for applications requiring high colour purity, such as LEDs. However, these materials typically suffer from low charge carrier mobility. Like nanowires, 1D perovskite structures,[9,10] can facilitate directional charge transport, although their fabrication and integration into devices remain technically challenging.[11] 2D perovskites comprise layered structures with alternating organic and inorganic components, where strong excitonic effects prevail due to the confinement of charge carriers. In contrast, 3D perovskites possess a continuous inorganic network with enhanced orbital overlap, which supports efficient and balanced transport of both electrons and holes.[12] The mixed-dimensional 2D/3D perovskite heterojunctions effectively combine improved stability with high efficiency.[13] Owing to quantum confinement, 2D perovskites exhibit a discrete absorption spectrum with sharp excitonic peaks and a blue-shifted absorption edge, whereas 3D perovskites display a broader absorption profile with a more gradual onset, reflecting their continuous band structure. At heterojunctions, exciton dissociation and free carrier generation are influenced by their optoelectronic properties, which impact charge transport and recombination dynamics.[14] Recombination processes, alongside energy funnelling[15] and cascading effects, further regulate carrier dynamics.

The differing transport mechanisms and emission characteristics of charged carriers and neutral excitons necessitate careful consideration in the design of optoelectronic and photonic devices.[16,17] Electron–phonon coupling plays a crucial role in hot carrier cooling, which occurs more rapidly in 2D perovskites than in 3D counterparts. In 2D/3D heterostructures, the cooling rate accelerates as the inorganic quantum well thickness decreases. This cooling mechanism is primarily governed by electron–phonon interactions, significantly affecting photon recycling and charge carrier lifetimes in perovskite-based optoelectronic devices.[18]

A well-coordinated interplay of photophysical processes—such as charge carrier dynamics, energy transport, exciton–phonon coupling, and exciton dissociation—is crucial for enhancing device efficiency, stability, and operational lifespan.[18,19]

In perovskite-based devices, interfaces critically govern charge transport,[20] with LD perovskites playing a key role in interface engineering for photovoltaic (Fig. 1(b)) and lighting applications (Fig. 1(c)). Integrating wide bandgap LD layers enhances performance by improving hydrophobicity, defect passivation, and ion migration.[21] Controlling crystal orientation[22] and phase distribution in solution-processed 2D/3D perovskite heterostructures enhances efficiency, reproducibility, and stability. Heterojunction growth and its quality, whether LD on 3D or *vice versa*, are strongly influenced by strain, surface states, inhomogeneities, and processing conditions.[23,24]

A deep understanding of structural and interfacial dynamics, along with controlled crystallisation[25] and growth of LD/3D heterostructures,[26] offers promising avenues for advanced multilayer architectures. Dielectric confinement in 2D perovskites, arising from low-permittivity organic spacers, strengthens Coulomb interactions, increasing exciton binding energy (E_b) and reducing free carrier generation. Spin–orbit coupling (SOC) from heavy metal cations further modulates electronic properties, while structural distortions from bond length and angle variations impact bandgap tuning.[27] Electrostatic interactions, such as dipole–dipole coupling between the organic spacers and inorganic layers, also influence E_b, where optimised dipole moments facilitate efficient charge dissociation and transport.[28] The incorporation of organic cations with extended conjugation promotes efficient charge and energy transfer across the organic–inorganic interface, tunes the exciton binding energy, improves charge carrier mobility, and enhances the intrinsic stability of the material.[29] These distinctions highlight the role of interface engineering in enhancing charge transport and energy transfer in 2D/3D perovskite heterojunctions as shown in schematic Fig. 1(d) and (e).

2. Lattice mismatch, ligand engineering and growth of the heterojunctions

Molecular stiffness and steric effects regulate phase formation, crystallisation, and crystal orientation in the perovskite systems.[34] The crystal structures of LD and 3D perovskites, which significantly influence charge carrier dynamics, have been extensively investigated (Fig. 2(a)–(c)). Lattice mismatch at the 2D/3D interface results from differences in in-plane lattice constants and structural incompatibility between the 3D isotropic framework and the 2D layered structure. Even small in-plane mismatches can accumulate strain at the interface, leading to distortions in the BX_6 octahedra, including bond tilting and stretching, which impact charge transport.[35] If the 2D perovskite's inorganic slab has a slightly smaller lattice constant than the 3D phase, the 2D layer undergoes tensile strain, while the 3D surface experiences compressive strain. Thin 2D layers (low *n*-values) or flexible organic spacers can partially accommodate this strain through elastic deformation. Additionally, mixing long and short alkyl chain ligands can balance tensile strain in perovskite films, reducing interfacial stress and enhancing structural stability.[36]

Lattice mismatch has been extensively studied by researchers, as shown in Fig. 2(d). It has been reported that

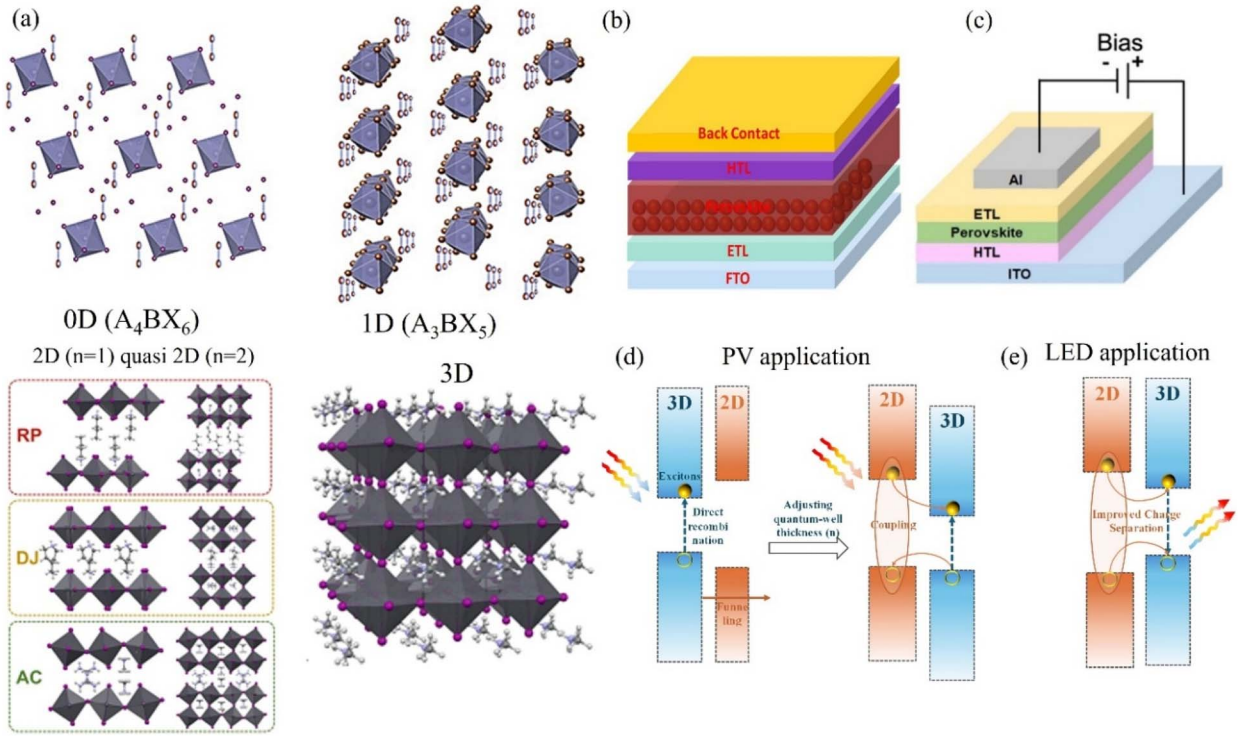

Fig. 1 (a) Schematic of 0D, 1D[30] and layered 2D and quasi-2D perovskite phases: Ruddlesden–Popper (RP), Dion–Jacobson (DJ) (reproduced from ref. 30 with permission from Wiley, copyright 2022 License CC BY 4.0), and alternating cations in interlayer (ACI) structures,[31] (reproduced from ref. 31 with permission from Springer Nature, copyright 2022 License CC BY 4.0). (b) Schematic stack structure of n–i–p perovskite solar cells,[32] reproduced from ref. 32 with permission from American Chemical Society, copyright 2023 License CC BY 4.0 (c) Device structure of a typical perovskite light-emitting diode (LED) device[33] (reproduced from ref. 33 with permission from American Chemical Society, copyright 2023 License CC BY 4.0), schematic illustration of different types of band alignment in vertical heterojunctions at 2D/3D perovskite interfaces for (d) photovoltaic (PV) applications, and (e) light-emitting diodes (LED) applications.

such mismatch can lead to the formation of surface states.[37] The higher and uneven surface potential of a 3D perovskite is dictated by its ionic nature, grain boundaries, surface defects (*e.g.*, undercoordinated Pb^{2+} or I^-), and termination (*e.g.*, PbI_2^- or MAI-rich). The potential difference creates an electrostatic attraction that initiates nucleation, with the organic cations anchoring to the 3D surface, followed by the assembly of inorganic BX_6 octahedral layers. When precursors for 2D perovskites (*e.g.*, large organic cations like butylammonium, BA^+, paired with PbI_2) are deposited, the higher surface potential of the 3D perovskite drives the adsorption of these cations. The organic spacers lower the surface energy by passivating defects[38] and forming a stable interface. A larger surface potential difference accelerates nucleation but may lead to heterogeneous growth if the 3D surface is uneven (*e.g.*, due to grain boundaries), potentially forming 2D phases with varying thicknesses (*n*-values).[34,39] The formation and crystallisation of the 2D phase on the 3D phase are also closely related to the molecular stiffness and steric hindrance of the ammonium group.[34,40] A slower crystallisation process helps achieve preferential orientation of the 2D phase.[41] GIWAXS analyses of 3D, 3D/2D, and 2D perovskite films at surface- (0.1°) and bulk-sensitive (0.2°) angles (Fig. 2(b), (c) and (e)–(g)) show that 3D and 3D/2D structures exhibit similar Bragg reflections with preferred orientation, whereas the 2D phases (γ and β) in the bilayers are predominantly located at the surface, textured out-of-plane, and display a broader angular distribution. Fig. 2(b) presents X-ray reflectivity (XRR), which provides information on the out-of-plane (specular) structure, film thickness, density contrast, and 2D/3D perovskite interface quality. The 2D component is primarily concentrated near the surface of the 3D/2D bilayer, based on the variation in Bragg peak intensities with penetration depth. This corresponds to roughly four layers of $(FEA)_2PbI_4$, estimated from the total film thickness (~8 nm) and its out-of-plane lattice spacing. Fig. 2(c) presents radially integrated GIWAXS/GIXD data, which probes the overall material crystallinity and the average crystal structure (phase identification) within a thin film, essentially giving a 1D powder X-ray diffraction pattern from a 2D image. The radial integration combines both in-plane and out-of-plane information. Together, XRR and GIWAXS offer complementary structural information.[21] *In situ* GIWAXS revealed the dynamic formation of the 2D/3D interface during vinylbenzylammonium bromide (VBABr) treatment of $MAPbI_3$ films, showing the transient appearance of an intermediate peak followed by the stable formation of the $n = 1$ phase. The diffraction features indicate that both intermediate and $n = 1$ species orient parallel to the substrate, consistent with low-*n* RP phases.[26]

The surface potential gradient at the 3D/2D interface influences the stacking direction of 2D perovskite layers. The

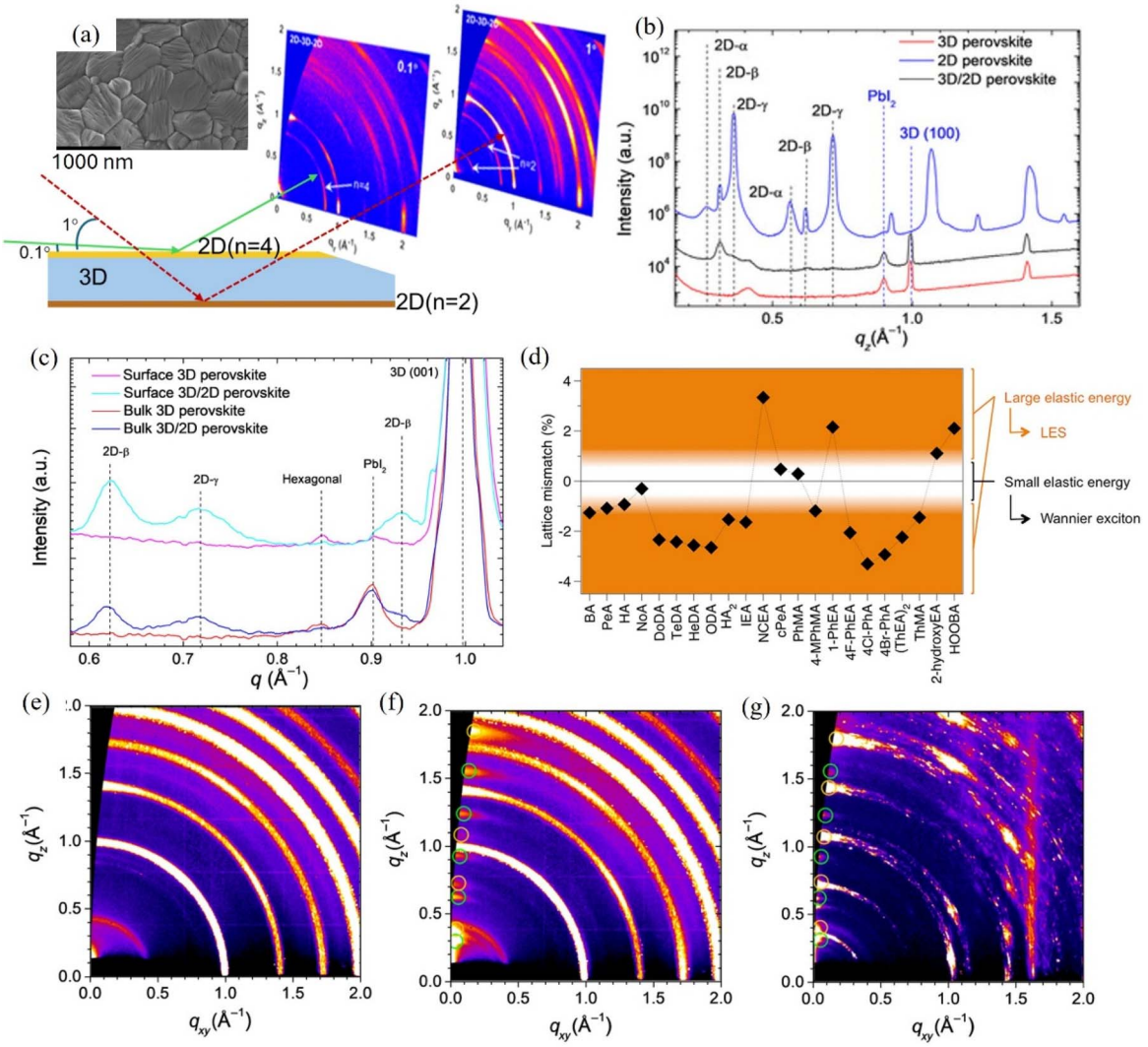

Fig. 2 Structural and morphological differences between 2D, 3D, and 3D/2D perovskite films using GIWAXS, XRR, SEM, and lattice mismatch analysis. (a) Illustration of GIWAXS (reciprocal maps for 2D/3D/2D perovskite for grazing incidence 0.1° and 1°, adopted from ref. 49 with permission from American Chemical Society, copyright 2024), Inset: SEM images of an FEAI-treated 3D/2D perovskite film, respectively.[21] (b) XRR data of pure 2D, 3D, and 3D/2D perovskite films. a.u. indicating arbitrary unit, (c) radially integrated GIWAXS intensity profiles collected at two incidence angles—0.2° for bulk sensitivity and 0.1° for enhanced surface sensitivity[21] (reproduced from ref. 21 with permission from Science, copyright 2019). (d) Lattice mismatch between different monolayered A'_2PbI_4 perovskites ($n = 1$) and $MAPbI_3$ ($I4cm$; $n = \infty$)[37] (reproduced from ref. 37 with permission from American Chemical Society, copyright 2018), and (e) to (g) reciprocal maps of 3D, 3D/2D, and pure 2D perovskite films (angle of incidence = 0.1°). Green and orange circles denote the 2D-β and 2D-γ structures, respectively.[21] (reproduced from ref. 21 with permission from Science, copyright 2019).

application of 2D perovskite for surface passivation transforms a large contact potential difference at the grain boundaries of 3D perovskite into a uniform potential distribution.[42] In addition, the grain boundaries of 3D perovskites serve as preferential sites for 2D phase nucleation, correlating with passivation mechanisms that enhance stability and efficiency in solar cells.[34] A surface planarisation approach is employed on the 3D perovskite to facilitate the epitaxial growth of a uniform 2D/3D perovskite heterojunction. A positively charged 3D surface (*e.g.*, PbI_2-terminated) attracts the negatively charged inorganic slabs of the 2D perovskite, aligning them parallel to the surface. This results in a 2D structure growing epitaxially on the 3D substrate.[43] The potential difference drives ion exchange or diffusion at the interface. For example, smaller cations (*e.g.*, MA^+) from the 3D perovskite may partially incorporate into the forming 2D layer, while larger organic cations penetrate the 3D surface, creating a graded interface. This dynamic is sensitive to processing conditions (*e.g.*, solvent polarity, annealing temperature), which modulate the surface potential. A significant potential mismatch can accelerate 2D growth but risks over-conversion of the 3D phase into 2D, reducing the bulk 3D properties critical for optoelectronic performance.[19] The 2D seed optimises the crystallisation kinetics of 3D perovskite, enabling its nucleation process to directly stride over the G^*, resulting in template-assisted growth.[34] The surface potential of a 2D perovskite is lower and more stable due to the organic

cation layer (*e.g.*, BA^+ or, PEA^+), which is hydrophobic and less reactive.[44] This low-energy surface poses a challenge for 3D perovskite nucleation, as it lacks the high-energy sites that are typical of 3D surfaces.[45] PEA_2PbI_4-based 2D perovskite is utilised as a substrate to grow the high-quality $CsPbI_3$ film. Due to a bottom-up self-diffusion process, PEA cations exhibit a vertical gradient distribution throughout the $CsPbI_3$ layer. PEA cations induce the moderate distortion of the $[PbI_6]^{4-}$ octahedron and slight lattice contraction of $CsPbI_3$ by chemically bonding between Pb and N atoms. If the inorganic BX_6 slabs are exposed (*e.g.*, in higher *n* 2D phases), the 3D perovskite can grow epitaxially, aligning its octahedral network with the 2D lattice. The well-matched energy levels at the interface, because of the gradual distribution, enhance hole transport.[46] The choice of the octahedron tilting through interlayer bond angle variance is possible by changing the organic cations.[47]

Tuning surface potential for improved heterojunctions in perovskites of different dimensionalities involves organic cation choice, surface treatments, and processing conditions like temperature and solvent polarity, which influence ion mobility and potential alignment.[44,48]

3. Energy band alignment

In 3D perovskites, charge transport is dictated by the continuous $[BX_6]^{4-}$ octahedral framework, where bond lengths (B–X) and angles (B–X–B) influence orbital hybridisation and electronic properties. Strong orbital overlap, such as Pb 6s–I 5p at the valence band maximum (VBM) and Pb 6p–I 5p at the conduction band minimum (CBM)[50] facilitates narrow bandgaps and efficient charge transport. High structural symmetry and uniform lattice arrangements further enhance charge mobility.[51,52] In contrast, 2D perovskites form quantum well (QW) structures,[53] where organic spacer cations disrupt orbital hybridisation, confining charge carriers and limiting cross-layer transport. The Pb–I–Pb bond angle and interlayer spacing, dictated by spacer cations, significantly influence the bandgap and charge mobility. Hydrogen bonding[19] and electrostatic interactions with halide ions induce lattice distortions, which, along with electron–phonon interactions (*e.g.*, Jahn–Teller effect),[7] generate localised energy states and enhance excitonic properties.

Optimising band alignment in 2D/3D perovskite heterojunctions as shown in schematic Fig. 1(d) and (e) is crucial for efficient charge transport and depends on alkyl and conjugated molecule selection and the 2D layer number (*n*-value). The band alignment in 2D/3D perovskite heterostructures can be tuned from Type-I to Type-II by adjusting the quantum-well thickness of the 2D perovskite layer. In Type-I band alignment, excitons funnel from larger bandgap (low-*n*) to smaller bandgap (high-*n*) regions, enhancing energy transfer, supporting radiative recombination, ideal for light-emitting applications. Conversely, Type-II band alignment not only facilitates effective trap passivation but also promotes efficient charge separation, which is essential for photovoltaic performance. The gradual shift in dimensionality, as well as the distribution of 2D phases within a 3D structure, reveals additional layers of control over band alignment.[54] 2D perovskite heterostructures are intrinsically prone to band misalignment due to thermal fluctuations and structural softness, which can lead to oscillatory band alignment between Type-I and Type-II at room temperature.[55] Feng *et al.*, using density functional theory (DFT), showed that reducing the 2D component favours Type-I alignment for energy funnelling, while a higher 2D ratio promotes Type-II alignment for charge separation.[56] Horizontally aligned $(PEA)_2PbBr_4/CsPbBr_3$ 2D/3D heterostructures tend to exhibit a Type-I, or otherwise unidirectional, energy-transfer pathway when the 2D perovskite layer is relatively thin. However, once the 2D layer thickness exceeds ~150 nm, the carrier-transfer characteristics shift and become more indicative of a charge-transfer-dominated Type-II mechanism.[57] The interspersed 2D/3D arrangement forms a p–n heterojunction with a built-in potential, which increases upon photoexcitation, influencing quasi-Fermi level splitting (QFLs). In cases where Type-I alignment forms in photovoltaic applications, the 2D layer must be sufficiently thin to enable charge tunnelling[19] and should primarily serve to passivate surface states. This separation enhances charge carrier lifetimes and is beneficial for photovoltaic devices. At the 2D/3D interface, excitons generated within the 2D layer can dissociate, releasing free carriers into the 3D phase, thereby increasing the overall carrier population available for band-to-band recombination. The alignment of interfacial energy is also notably influenced by the confined dipoles of spacer cations and the nature of the perovskite surface termination. The band alignment differs depending on whether the termination involves an inorganic octahedron or organic cations.[58,59]

The ability to manipulate Type-I and Type-II band alignments through structural engineering offers versatility in applications ranging from high-efficiency photovoltaics to next-generation LEDs.[54]

4. Energy transfer processes

LD perovskites typically have quantum-confinement effects due to their restricted dimensionality, leading to higher exciton binding energies and larger bandgaps compared to 3D perovskites.[1,60] This makes LD perovskites excellent energy donors in a heterojunction with 3D perovskites. Energy transfer typically proceeds through two primary pathways: FRET and DET. FRET operates as a long-range dipole–dipole interaction, generally associated with singlet–singlet states,[61] while DET is a short-range electron-exchange process that can engage triplet–triplet states and singlet–singlet states.[62] In LD to 3D or 3D-like perovskites, transfer may occur *via* FRET[63,64] (Fig. 3(a and b)) or DET, depending on the separation and interaction between the two phases.

When light is absorbed by the LD perovskite (*e.g.*, a 2D perovskite layer), excitons (bound electron–hole pairs) are created due to the material's high exciton binding energy. The driving force for this energy transfer is the bandgap difference, where the larger bandgap of the LD perovskite allows excitons to transfer their energy to the smaller bandgap 3D perovskite. This process enhances the overall light-harvesting efficiency in solar cells. Generally, two types of excitons are observed in

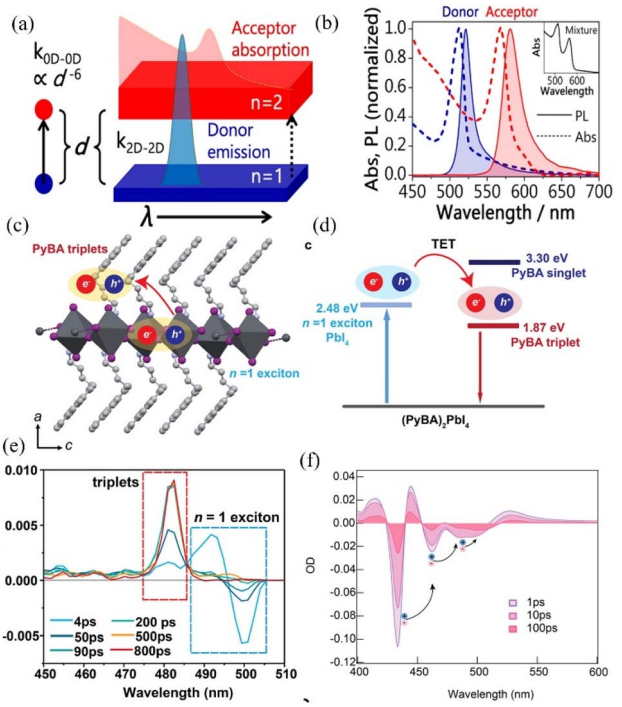

Fig. 3 The mechanisms of energy transfer in quasi-2D perovskites, highlighting how structural design and spectral alignment enable efficient exciton funnelling across layered domains. (a) FRET typically refers to the non-radiative energy transfer between donor and acceptor molecules modelled as point dipoles, with the transfer rate (k_{0D-0D}) inversely related to the sixth power of the distance d between them. In the case of 2D perovskite quantum wells, the in-plane spatial extension and appropriate spectral overlap are proposed to enhance energy transfer rates (k_{2D}–k_{2D}), potentially due to a higher effective density of acceptor sites. (b) Absorption and photoluminescence (PL) spectra corresponding to the donor phase ($n = 1$) and acceptor phase ($n = 2$) of the quasi-2D perovskite system $(BA)_2MA_{n-1}Pb_nI_{3n+1}$ are shown, highlighting their distinct optical characteristics[64] (reproduced from ref. 64 with permission from American Chemical Society, copyright 2021), structural analysis and band alignment: (c) illustration of the $(PyBA)_2PbI_4$ crystal structure, representing an $n = 1$ two-dimensional perovskite incorporating pyrene-based PyBA ligands. (d) Comparison of exciton energy levels between the lead-iodide layer (donor) and the pyrene moiety (acceptor), indicating the energetic favourability for TET across the inorganic–organic interface. (e) Transient absorption spectra of the $(PyBA)_2PbI_4$ film recorded at various time delays following selective excitation of the PbI_4 framework[68] (reproduced from ref. 68 with permission from American Chemical Society, copyright 2024). (f) Transient absorption spectra of energy-landscape-engineered quasi-2D perovskite films ($n \geq 3$), comprising multiple domains through which energy is funnelled toward the terminal $n = 5$ phase[72] (reproduced from ref. 72 with permission from American Chemical Society, copyright 2017).

semiconductors, namely Wannier and Frenkel excitons.[16] The Wannier excitons are stretched over the host by numerous lattice constants with small binding energies of <100 meV, whereas the Frenkel excitons have large binding energies of ~500 meV, which are tightly bound to a single unit cell. Most of the reports suggest the presence of the Wannier-type exciton in 2D perovskites, although no consensus on the nature of excitons in 2D perovskites has been reached. A direct measurement yielded two excitonic features well separated from continuum for BA_2PbI_4.[65] Reports on PEA_2PbI_4 indicate the presence of Wannier-type excitons, although further investigations are still needed to fully clarify the interplay between Frenkel and Wannier excitonic behaviour. In 2D layered perovskites, excitons exhibit a dual character: Frenkel-like localisation along the stacking axis, combined with Wannier-like delocalisation within the inorganic 2D plane. A notable feature is their strong interaction with a longitudinal optical (LO) phonon mode of approximately 17 meV, which dominates the PL linewidth broadening. These findings emphasise the necessity of accounting for the intricate exciton–phonon coupling mechanisms when analysing the optoelectronic properties of 2D layered perovskites.[66] Almost ideal Dexter-type TET between Wannier excitons in inorganic $PbBr_4^{2-}$ perovskite layers and naphthalene molecules in the organic layer is reported by Ema *et al.*[67] This transfer has shown an exponential dependence on the separation distance, which was controlled by the length of the tethering alkylammonium group that links the naphthalene moiety to the inorganic layers. The $\Gamma_{1,2}^-$ excitonic states display comparatively long decay times on the order of 1–10 ns, consistent with their stabilised excitonic character in these quantum-confined structures. Upon interfacing with naphthalene molecules, both the rate and efficiency of energy transfer become highly sensitive to the spatial separation between the inorganic exciton and the organic acceptor. In the reported N–C1 configuration, the transfer efficiency approaches unity, exceeding 99%, which demonstrates highly effective exciton extraction. Furthermore, the observed near-exponential dependence of the energy transfer rate constant on the donor–acceptor distance indicates that short-range exchange interactions dominate, identifying Dexter-type energy transfer as the primary mechanism.[67] Careful engineering of the organic–inorganic interfaces in 2D hybrid perovskites enables efficient TET (Fig. 3(c)–(e)), primarily driven by exciton quantum tunnelling.[68] Luo *et al.* have explored the role of quantum confinement in TET for inorganic perovskite nanocrystals.[69] While LD perovskites can efficiently absorb light and generate excitons, their high exciton binding energy can limit free charge generation. For the $n = 3$ Ruddlesden–Popper perovskite structure, the excitonic diffusion constant has been measured to be approximately 0.18 $cm^2\ s^{-1}$.[70] However, when excitons transfer energy to the 3D perovskite, they can dissociate into free carriers (electrons and holes) more easily due to the lower binding energy in 3D perovskites. This exciton dissociation in the 3D perovskite domain boosts charge carrier generation, improving the device's photoelectric conversion efficiency. The 2D/3D perovskite structure supports cascading energy transfer by driving energy from wide bandgap to narrow bandgap regions, limiting free charge diffusion and increasing electron and hole densities. This process enhances radiative recombination by promoting higher band-to-band interactions. PL and transient absorption spectroscopy (TAS) measurements confirm energy cascading in GABr-treated perovskite films, evidenced by new bleach features and red-shifted exciton peaks. Distinct 2D absorption at ~413 nm and ~440 nm ($n = 2$, 3) and strong PL from the $n = 3$ phase indicate efficient energy funnelling from

wider to narrower bandgap regions.[71] However, localised 2D perovskite distributions cause inconsistent energy alignment, which could unavoidably introduce traps or defects, adversely affecting the charge transfer.[54] By carefully controlling the composition to form quasi-2D structures, it is possible to promote rapid energy transfer into the lower-bandgap minority phases, thereby reducing losses to non-radiative recombination, as illustrated in Fig. 3(f).[72] In a heterostructure composed of PEA_2PbI_4 ($n = 1$) and $PEA_2(MA)Pb_2I_7$ ($n = 2$), energy transfer occurs from the lower-n ($n = 1$) layers to the higher-n ($n = 2$) layers following photoexcitation. This interlayer energy transfer takes place on a timescale of $\sim 10^2$ ps, reflecting efficient excitonic coupling and directional energy funnelling across the mixed-dimensional interface.[73] In mixed-dimensionality perovskite structures, the rate of energy transfer increases as the layer number rises from $n = 3$ to $n = 5$ and beyond. The energy transfer occurs on an ultrafast timescale of less than 1 ps, and studies also report charge cascading from $n = 3$ to $n > 5$ phases.[74]

In 2D perovskites, dielectric confinement originates from the mismatch between the dielectric constants of the inorganic framework and the organic spacer layers. Incorporating 2-(4-(cyanophenyl)benzothiazol-2-yl)ethylammonium (CNBThMA) as a semiconducting spacer has been shown to mitigate this mismatch: its large dipole moment effectively balances the dielectric disparity, while its face-to-face stacking arrangement improves organic layer organisation and overall film morphology, leading to enhanced photovoltaic efficiency.[75] The presence of dielectric confinement amplifies the influence of quantum confinement, further increasing the exciton binding energy and reducing the effective electron–hole pair size, even in the absence of physical dimensional reduction.[76] Building on this concept, efficient blue LEDs have been realised using colloidal, quantum-confined 2D perovskites with stacking precisely controlled to the single-unit-cell level ($n = 1$). Embedding these 2D layers in low-k organic host matrices effectively creates a system of dielectric quantum wells, which substantially boosts the exciton binding energy *via* dielectric confinement. Energy funnelled through FRET is subsequently radiatively recombined within the 2D perovskite domains, delivering bright and stable emission.[77]

The length of the alkyl chain plays a crucial role in determining both the exciton type and the energy transfer mechanism in 2D perovskites.[64] The energy landscape at the 2D/3D interface is largely influenced by the choice of organic cation, as the size of the cation affects the positioning of the inorganic octahedra.[67] While many studies point to the presence of Wannier-type excitons or Frenkel–Wannier hybrid excitons, their exact nature remains a topic of debate. Irregularities in phase distribution can hinder the smooth energy cascade, negatively impacting overall device efficiency.[78] These insights highlight the importance of precise interface engineering in LD/3D perovskite heterojunctions.

5. Charge transfer processes

Charge transfer refers to the movement of electrons and holes between LD and 3D perovskite layers . This process is crucial for extracting/injecting carriers in devices such as solar cells and LEDs.[79] While 2D perovskites exhibit strong exciton binding energy, excitons transferring to adjacent 3D layers can generate free charge carriers. Mixed-dimensional perovskites with higher n-values enhance charge separation due to their lower exciton binding energy (E_b). Additionally, the built-in electric field at the 3D/2D p–n junction facilitates hole extraction and quasi-Fermi level alignment.[80,81] The energy level alignment between 2D/3D perovskite, which changes upon illumination, is shown in Fig. 4(a).[82] At the 2D/3D interface, excitons generated in the 2D layer can dissociate, enabling electrons and holes to transfer into the 3D phase driven by favourable band alignment and built-in electric fields, thereby facilitating efficient charge separation. These carriers are subsequently extracted into the respective electron and hole transport layers. Their transport behaviour can be probed using single-carrier devices, as shown in Fig. 4(b) and (c). Optimising charge transfer at the LD/3D interface requires precise heterojunction engineering to minimise potential barriers and defects.[83] The dipole moment of the organic cation influences the internal electric field, and when band bending is suitably tuned, it can facilitate efficient charge transport within the device.[84] Additionally, the nature of the organic cation plays a key role in determining the extent of quantum confinement, which in turn affects carrier mobility. Due to these confinement effects, LD perovskites generally exhibit lower carrier mobility compared to their 3D counterparts. In 2D organic–inorganic perovskites, reduced in-plane charge mobility and broad emission are primarily attributed to structural factors such as gauche conformations and distortions within the organic cation chains.[85]

To optimise charge transport properties, aligning 2D perovskite flakes with respect to the substrate is important.[86] The bulky organic cations in 2D perovskites hinder charge transport in a parallel configuration, necessitating hopping across long-chain organic ligands. In contrast, vertical stacking enables a direct transport pathway, improving charge transfer efficiency. Low charge mobility in 2D halide perovskites is primarily influenced by electron–phonon scattering, as observed in temperature-dependent microwave conductivity studies of $BA_2MA_{n-1}Pb_nI_{3n+1}$ systems.[87] However, as the n-value increases, charge transport begins to resemble 3D behaviour, suggesting that dynamic disorder significantly impacts the local crystal structure and charge mobility. Strong electron–phonon coupling in 2D perovskites leads to small polaron formation and local lattice distortions, which hinder efficient band-edge transport and result in hopping-like transport. While this limits charge mobility, it enhances broadband emission, making 2D perovskites promising for white-light LEDs. However, the precise nature of phonon interactions affecting charge mobility remains under debate.[88] Lattice distortions at the heterojunction contribute to energy dissipation by non-radiative processes. Engineering the lattice to minimise exciton–phonon coupling, for instance, could reduce non-radiative losses and enhance charge transport.[89] Minimising polaron formation in 2D/3D perovskite heterojunctions is crucial for enhancing charge transport efficiency and device performance.

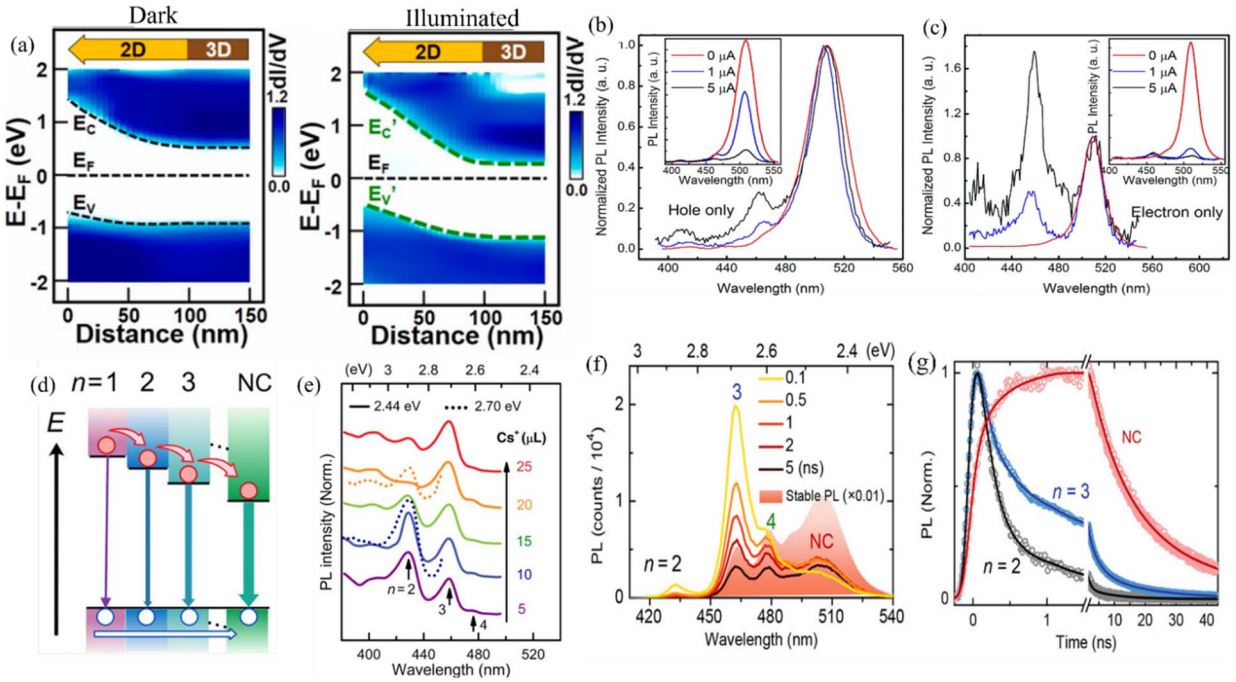

Fig. 4 The figure highlights band alignment and carrier dynamics across 2D/3D perovskite interfaces, showcasing charge transfer and recombination behaviour in layered and nanocrystal domains. (a) Spatially resolved band alignment maps across 2D/3D perovskite heterointerfaces, shown in dark conditions and under 515 nm illumination, reveal the evolution of local electronic states. The conduction band minimum (E_C), valence band maximum (E_V), and Fermi level (E_F) are indicated[82] (reproduced from ref. 82 with permission Elsevier Ltd, copyright 2021). (b) PL spectra measured under hole-only electrical injection, showing relative enhancement of lower-n emission features with increasing current. (c) PL spectra under electron-only injection, exhibiting stronger cascade behaviour compared to hole-only case. Insets in (b) and (c) show PL spectra under different current levels.[63] (reproduced from ref. 63 with permission Elsevier Ltd, copyright 2018). (d) Illustration of carrier transfer pathways across multiple quantum wells (MQWs) in quasi-2D perovskites with different layer thicknesses (n = 1–3) and nanocrystals (NCs).[90] (e) PL excitation spectra, showing PL peaks at 2.44 eV (NC resonance, solid lines) and 2.70 eV (n = 3 resonance, dotted lines).[90] (f) Steady-state PL spectra of $PA_2(CsPbBr_3)_{n-1}PbBr_4$ films with varying Cs^+ dose showing the evolution of emission from low-n to NC phases, along with time-delayed steady-state PL spectra revealing the spectral dynamics of the MQW components.[90] (g) Time-resolved PL decay curves of representative phases, highlighting faster recombination in NCs[90] (reproduced from ref. 90 with permission from John Wiley and Sons, copyright 2018).

In 2D perovskites, strong electron–phonon coupling can lead to the formation of small polarons, which are more localised and have lower mobility. This localisation can trap carriers, reducing their ability to participate in charge transport across the 2D/3D interface. The formation of polarons introduces delays in charge transfer across the heterojunction. Since polarons are heavier and less mobile, they require more energy to move across the interface, which can slow down the overall charge transport process.[18]

Milot *et al.* investigated charge transport in 2D perovskites by varying the MA-to-PEA ratio in $MA_{n-1}PEA_2Pb_nI_{3n+1}$ thin films. Their findings highlight a trade-off between crystal orientation and charge transport efficiency.[91] Faini *et al.* reported that hole transfer from the $n = 3$ to $n = 1$ phase occurs within tens of picoseconds, whereas electron transfer is more constrained due to the high exciton binding energy and low diffusion in the $n = 1$ phase.[92] Fluorination of PEA cations effectively modulates charge and energy transfer in heterostructures.[93] Considering mixed-dimensional 2D/3D perovskite, photo-induced carrier blocking is observed because of the high built-in potential.[94] SOC affects the electronic structure and charge carrier dynamics[95] in LD and 3D perovskites. SOC also affects the asynchronous charge transport in 2D perovskite[96] along with a reduction in bandgap,[27] while in 3D perovskites, SOC accelerates the nonradiative relaxation of hot carriers, contributing to longer-lived charge carriers.[97] Improved carrier lifetime is observed for 2D/3D/2D heterostructures.[98]

In well-engineered LD/3D heterojunctions, charge-carrier tunnelling across the interface can occur when the LD perovskite layer is sufficiently thin, thereby minimising recombination losses. Under such conditions, the LD layer can simultaneously improve environmental stability and light absorption without significantly hindering charge transport. For example, the insertion of a self-assembled 2D BA_2PbBr_4 tunnelling layer between SnO_2 and the 3D perovskite in wide-bandgap perovskite solar cells effectively reduced carrier losses associated with band alignment mismatch.[99] Similarly, 1D–3D hybrid structures exhibit improved charge transport due to favourable interfacial energetics, reflected in a marked reduction in the carrier transport time constant (from ~1.6 to ~1.1 microseconds), indicating more efficient carrier extraction and suppressed recombination.[100] In contrast, 0D perovskites display distinctly different optoelectronic behaviour compared with other reduced-dimensional systems. The presence of

electronically isolated metal-halide clusters results in strong quantum confinement, leading to higher exciton binding energies and pronounced carrier localisation. In Na-alloy-engineered 3D/0D metal-halide heterostructures, efficient charge transfer from the 3D phase to the 0D phase has been demonstrated (*e.g.*, $Cs_2NaLuCl_6$ (3D)/Cs_3LuCl_6 (0D)). The formation of the 3D/0D heterostructure also results in a shorter PL lifetime compared to the pristine 3D phase, confirming enhanced interfacial charge transfer. The increased charge density in the 0D phase further promotes energy transfer from $[LuCl_6]^{3-}$ to $[SbCl_6]^{3-}$, which enhances the self-trapped exciton emission of the 0D acceptor. Notably, direct energy transfer between $[SbCl_6]^{3-}$ units across the 3D and 0D phases is suppressed due to the narrow excitation window associated with the $[SbCl_6]^{3-}$ species.[101]

Electron–phonon coupling plays a dual role in charge transport across 2D/3D perovskite heterojunctions.[88] While excessive coupling can hinder mobility and interfacial transfer through scattering and polaron formation, moderate coupling facilitates energy dissipation and improves device performance when properly engineered.[18] At the 2D/3D interface, the transition in coupling strength can create a bottleneck for charge transport. Dipole moment of the organic cations can be tailored to improve band bending for improved charge extraction.[59]

Overall, these examples highlight that while LD perovskites including 1D and 2D can preserve efficient charge transport through interfacial tunnelling and favourable band alignment,[99] 0D perovskites operate *via* fundamentally different, confinement-driven charge transfer pathways, underscoring the critical role of dimensionality in dictating transport efficiency, recombination dynamics, and optoelectronic functionality in perovskite heterostructures.[8,101]

6. Synergistic interplay between energy and charge transfer

Interlayer charge transport in 2D/3D perovskites is influenced by interfacial scattering, defect trapping, and exciton localisation. These interactions critically affect exciton dissociation rates and charge carrier dynamics, directly impacting optoelectronic performance. Strong excitonic effects in 2D perovskites enhance electron–phonon coupling, influencing carrier mobility, hot-carrier relaxation, and emission broadening.[86,102] Studies reveal a complex interplay between TET and charge trapping,[103] with sub-picosecond hole transfer driving triplet sensitisation instead of conventional Dexter transfer mechanisms.[104] Both energy and charge transfer processes have been observed to coexist in 2D/3D hybrid perovskites, featuring an exceptionally fast initial transfer occurring in under 100 femtoseconds, followed by a slower transfer pathway lasting between 2 to 15 picoseconds. Femtosecond energy transfer is fast enough to move excitons out of high-binding-energy 2D regions before they recombine, enabling more efficient charge separation and collection in 2D/3D perovskite solar cells.[89,105] This rapid transfer is attributed to the strong coupling between the distinct perovskite phases (Fig. 4(d)–(g)).[82,90,106]

6.1. Energy transfer enhancing charge generation

Energy transfer from the 2D to the 3D perovskite domain enhances free charge generation in the 3D phase, which, due to superior transport properties (Fig. 5(a)), efficiently separates and directs charges toward electrodes. Wang *et al.* identified two distinct processes in 2D/3D $CsPbBr_3$ hybrids: a fast hot-carrier relaxation and a slower energy transfer from 2D to 3D, extending charge carrier lifetimes (Fig. 5(b) and (c)). TRPL and TAS confirmed that this transfer affects ground-state bleaching and contributes to improved device performance.[107] Photons

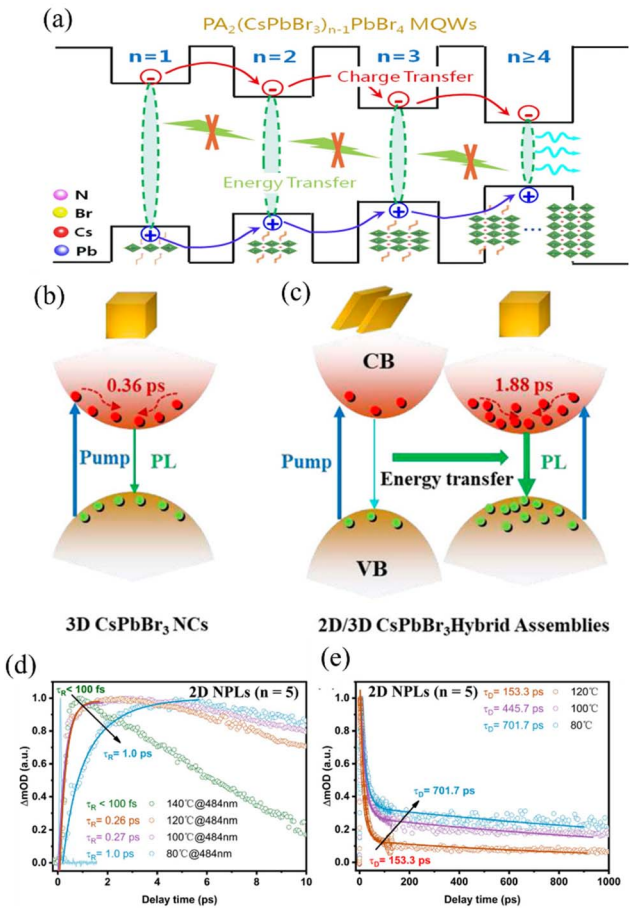

Fig. 5 The figure illustrates energy and charge transfer across $CsPbBr_3$ quantum wells and hybrid 2D/3D assemblies, highlighting Förster-type exciton funnelling and dynamic carrier transfer from lower-to higher-*n* phases. (a) Band diagram of $PA_2(CsPbBr_3)_{n-1}$ $PbBr_4$ MQWs illustrating energy transfer (green arrows) and electron charge transfer (red arrows) between quantum wells of different *n* value[63] (reproduced from ref. 63 with permission from Elsevier Ltd, copyright 2018). (b and c) Schematic representation of Förster-type energy transfer in 2D/3D $CsPbBr_3$ hybrid structures, where photoexcited carriers in the 2D nanoplatelets nonradiatively transfer energy to adjacent 3D nanocrystals. (d) The rise and decay (e) times of the ground-state bleaching (GSB) signal for 2D $CsPbBr_3$ nanoplatelets ($n = 5$) at 484 nm under varying reaction temperatures. T_R denotes temporal resolution; τ_R is the rise time; and τ_D is the decay time. The extended rise time of the GSB signal suggests energy transfer from lower-*n* phases ($n = 2$, 3, and 4) to the $n = 5$ phase within the 2D $CsPbBr_3$ hybrid structures[107] (reproduced from ref. 107 with permission from AIP publishing, copyright 2024).

absorbed by 2D layers generate photocurrent *via* energy transfer to the lower-bandgap 3D-like phase (Fig. 5(d) and (e)), which primarily governs charge transport. This interplay effectively bridges small-*n* 2D and 3D-like phases, promoting efficient carrier extraction and reducing charge accumulation, thereby minimising recombination losses. While phase distribution and band alignment complexities introduce intricate energy landscapes, influencing charge and energy funnelling, phase composition adjustments alter carrier transport pathways, with small-*n* phase accumulation doubling the carrier diffusion coefficient (from 0.085 to 0.20 $cm^2 s^{-1}$) and extending diffusion length by 1.5 times. The phase-order engineering further enhances charge separation, underscoring the role of molecular and structural design in optimising perovskite optoelectronic performance.[108]

6.2. Charge transfer enhancing radiative recombination

The broad *n*-phase distribution in quasi-2D perovskites leads to inefficient charge transport, broadening the luminescence and introducing parasitic emissions. While quasi-2D structures improve luminescence efficiency, they also create complex low-dimensional phase distribution issues. Layered 2D halide perovskites suffer from nonradiative carrier losses, particularly under high carrier injection fluences, due to many-body interactions such as Auger recombination and exciton–exciton annihilation (EEA). Compared to 3D perovskites, 2D systems exhibit faster EEA and Auger recombination due to their high exciton binding energies and strong coulombic interactions.[88] Surface and grain boundary (GB) passivation of DMA^+ (dimethylammonium) creates a 2D/3D hybrid heterojunction. This enhances charge transfer while suppressing trap-assisted nonradiative recombination.[109] Introducing high-polar organic cations, such as *p*-fluorophenethylammonium (*p*-$FPEA^+$), at the A-site reduces exciton binding energy (E_e), lowering the Auger recombination rate by an order of magnitude and improving efficiency.[110] In quasi-2D films, efficient energy transfer concentrates photoexcited states into radiative domains, allowing bimolecular radiative recombination to dominate over defect trapping. This enhances photoluminescence quantum yield (PLQY), making these materials promising for high-efficiency optoelectronic applications. Additives like methanesulfonate (MeS) further optimise energy transfer by promoting structural reconstruction and defect reduction, mitigating nonradiative recombination and enhancing overall device performance.[111] The efficiency of charge and energy transfer in LD/3D perovskites depends on interface quality, as interfacial traps can cause recombination losses. Molecular dipole moment engineering offers a solution by tuning energy levels and built-in potential (V_{ei}) in 3D/2D heterojunctions. Integrating passivating dipole layers (PDLs), such as 4-methoxyphenylphosphonic acid (MPA), improves band alignment and electron extraction in p–i–n perovskite solar cells.[112]

Efficient conversion between excitons and free charges is key to the high performance of the optoelectronic device. Strategic structural engineering, defect passivation, and interface optimisation are essential for controlling carrier dynamics and minimising nonradiative losses.[109] *These advancements pave the way for high-performance, next-generation optoelectronic devices.*

7. Role of heterojunctions in perovskite devices

In exploring the impact of LD/3D heterojunctions on solar cell[113] and LED performance, a significant opportunity emerges for enhancing both power conversion and light-emission efficiency (Fig. 6).[114] The carrier dynamics management at 2D/3D heterojunctions can be effectively achieved through molecular engineering. One promising strategy involves designing π-conjugated organic cations, which not only promote the formation of stable 2D perovskites but also enable precise tuning of the energy levels at the 2D/3D interfaces. This tailored alignment facilitates reduced hole-transfer energy barriers across the heterojunction and within the 2D domains. Furthermore, the associated work-function modulation minimises interfacial charge accumulation, thereby enhancing overall device efficiency.[115] In LEDs, this LD/3D interaction enhances light emission by directing energy from the LD to the 3D layer, leading to increased brightness and improved colour purity, making these heterojunctions particularly beneficial for high-luminescence applications such as display and lighting technologies. In these perovskite systems, fine tuning of the crystal structure,[116] optimising exciton energy transfer and minimising deep defect states is essential for achieving high emission efficiency. In conventional n–i–p PSCs, a Type-II band alignment naturally forms between the 3D and 2D layers due to the broad bandgap and high valence band position of 2D perovskites. This alignment acts as an effective electron-blocking barrier, enhancing both open-circuit voltage (V_{oc}) and fill factor (FF). However, in inverted p–i–n PSCs, the 3D/2D junction introduces a high energy barrier for electron extraction, impeding charge transport to the ETL and reducing efficiency. α-$FAPbI_3$ has gained massive interest in recent years.[117] *In situ*-formed 2D perovskites can regulate nucleation (Fig. 6(a)) and promote the oriented crystal growth of α-$FAPbI_3$-rich films, leading to high-quality films with lower trap densities and extended carrier lifetimes, achieving power conversion efficiencies as high as 26.16%.[118] Zhang *et al.* have reported excellent stability of high performance solar cells involving 2D/3D/2D structures (Fig. 6(b)–(d)).[98] Tin (Sn) offers a more environmentally sustainable alternative to lead (Pb), yet tin-based perovskites tend to suffer from reduced stability. Employing a layered LD perovskite structure can help mitigate degradation caused by self-doping and limit the oxidation of Sn^{2+}, thereby enhancing the material's overall durability.[119] Carefully selected long-chain or bulky organic ligands with aromatic rings—capable of forming π–π stacking—help stabilise the layered structure, mitigate energy barriers and thereby resulting solar cells with efficiencies as high as 25.7%.[120] Heterostructures combining 2D and 3D perovskite phases, often achieved through long-chain organic ammonium post-treatments, on 3D perovskites have shown remarkable improvements in perovskite LED (PeLED) performance. The solution-based process

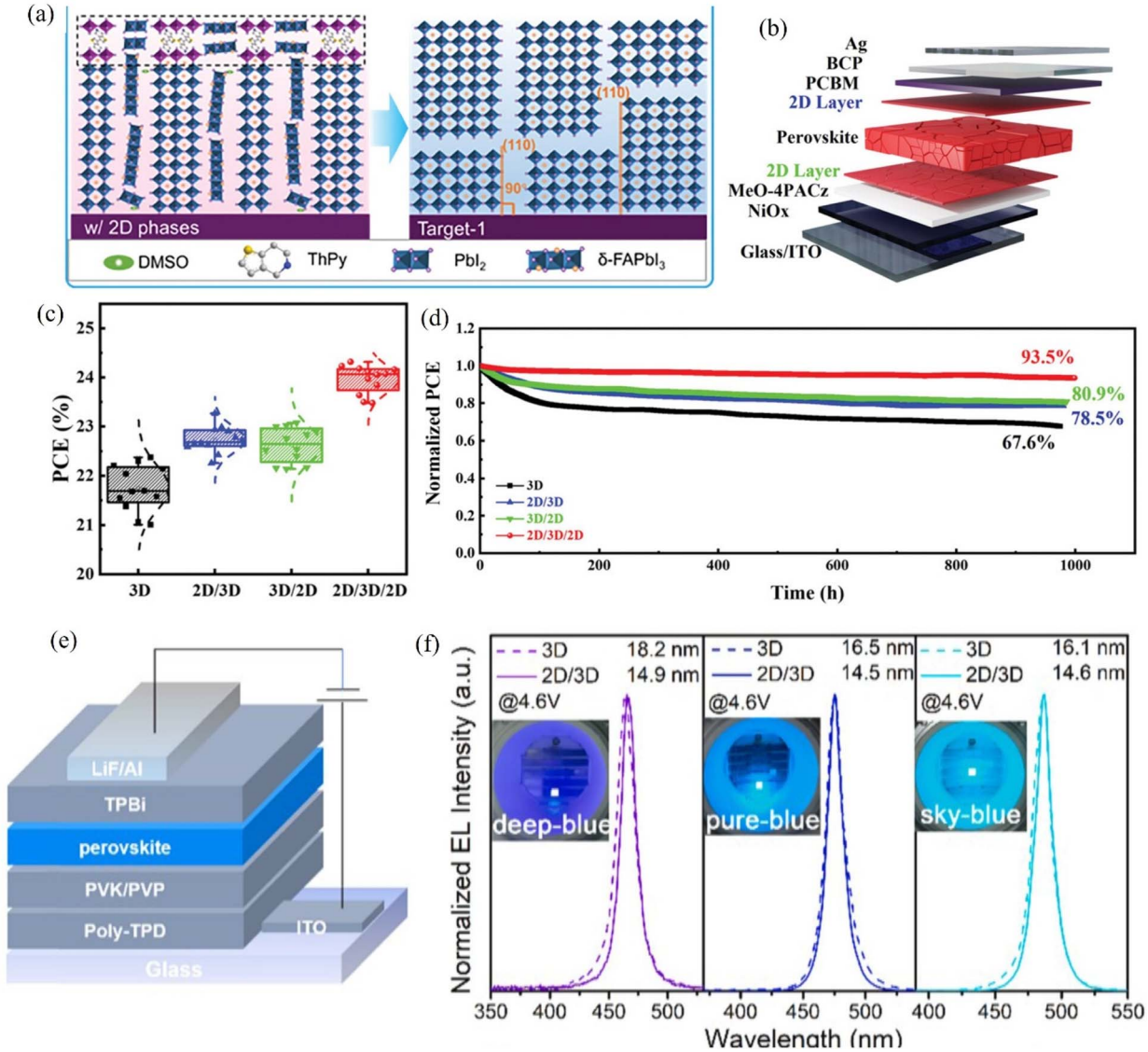

Fig. 6 Device performance and stability. (a) Schematic depiction of the 2D-perovskite-assisted controlled growth (2D-ACG) approach, where *in situ* formation of 2D phases guides the crystallisation of the perovskite film[118] (reproduced from ref. 118 with permission from John Wiley and Sons, copyright 2024). (b) Cross-sectional view of the device featuring 2D/3D/2D perovskite along with the transport layers and contacts. (c) Box plots summarising the statistical distribution of PCE values across devices employing different perovskite configurations. (d) MPP stability monitoring of encapsulated devices incorporating various perovskite architectures, measured under 1-sun illumination in ambient air at room temperature.[98] (reproduced from ref. 98 with permission from John Wiley and Sons, copyright 2023). (e) Schematic of the device architecture based on 3D or 2D/3D perovskites as emissive layer. (f) EL spectra of 3D and 2D/3D perovskites based PeLEDs with varying emission peaks. Insets are corresponding photograph of PeLED under constant voltage[121] (reproduced from ref. 121 with permission from Elsevier Ltd, copyright 2022).

enables the formation of a thin low-dimensional capping layer, which not only enhances radiative recombination efficiency but also promotes better crystallisation of the perovskite film by reorganising the surface. Moreover, such treatments yield homogeneous mixed-halide 2D/3D structures with improved colour saturation, a factor crucial for maintaining electroluminescence (EL) stability. These structural and optoelectronic benefits translate into ultra-low turn-on voltages, efficient charge injection, and highly effective radiative recombination, leading to high brightness and excellent external quantum efficiencies (EQEs). Notably, 2D/3D perovskite engineering has enabled tunable blue PeLEDs with competitive performance, addressing one of the key challenges in perovskite optoelectronics (Fig. 6(e) and (f)).[121] Furthermore, incorporating low-dimensional phases into 3D perovskites ensures stable EL under applied biases, supporting long-term operation without wavelength shifts or peak splitting, as demonstrated by Lin *et al.* in red LEDs. For instance, the EL spectra reported under varying voltage injections clearly illustrate the stable emission of devices employing $PA_2CsPb_2I_7$ as the active layer.[122] These findings highlight the importance of tailored LD/3D configurations to meet the specific functional demands of solar cells and LEDs.

The integration of LD/3D heterojunctions presents a promising strategy for enhancing both power conversion efficiency in solar cells and light-emission efficiency in LEDs. In solar cells, LD perovskites improve stability and facilitate an optimal balance of energy and charge transfer within the 3D structure. The 3D perovskite layer serves as the primary charge transport channel, complementing the stability of LD perovskites, resulting in more durable and efficient devices with improved environmental resilience.[123,124]

7.1. Impact on stability and performance

Beyond optimising energy and charge transfer, LD perovskites significantly enhance device stability.[134] Their layered structure provides superior resistance to environmental stressors such as moisture, heat, and oxygen, acting as a protective barrier for the underlying 3D perovskite layer.[124] By passivating surface defects[84] and shielding against degradation, the LD layer improves long-term operational stability without compromising charge or energy transfer.[135] Among LD perovskites, DJ and ACI types exhibit greater stability than RP perovskites due to reduced or absent van der Waals forces within spacer cation bilayers and shorter interlayer distances.[31] Hydrogen bonding between spacer cations and inorganic slabs further reinforces structural integrity, enhancing resistance to environmental degradation.[136] He *et al.* demonstrated that 1-ethyl-3-methylimidazolium tetrafluoroborate ($EMIMBF_4$) converts excess PbI_2 into robust 1D $EMIMPbI_3$, which withstands lattice strain while forming an interfacial dipole layer at the SnO_2/perovskite interface. This reconfigures the interfacial energy band, accelerating charge extraction while maintaining high efficiency and excellent stability.[133] Dipropylammonium iodide, a compact yet bulky secondary ammonium cation, facilitates the formation of the perovskite layer that exhibits longer carrier lifetime, enhanced thermal stability, and strong resistance to heat-induced degradation.[137] Spacer cation steric effects influence the spatial arrangement, orientation, electrical conductivity, and optoelectronic properties of layered perovskites. The incorporation of large cations as additives and for surface termination effectively passivates surface defects, enhances stability against humidity-induced degradation, and minimises ion migration[21] by stabilising both cations and halide anions (Fig. 6(a) and (d)). It is noteworthy that studies have reported the formation of a quasi-2D graded perovskite structure at the 2D/3D heterojunction over time, while maintaining solar cell performance.[134] As LEDs operate at higher voltages than solar cells, ion migration is naturally more pronounced in these devices. The incorporation of 2D or quasi-2D perovskites in LEDs helps to reduce intergrain ion migration, although the devices remain somewhat susceptible.[138] Directionally aligned and well-ordered phase distributions facilitate efficient carrier transport, whereas disordered or randomly distributed phases introduce trap states and localised charge accumulation that accelerate material degradation. The same phase landscape that governs exciton funnelling therefore also dictates ionic transport and long-term stability. In particular, a smoothly graded distribution from low-*n* to high-*n* quantum wells establishes continuous energy cascades,[134] reducing carrier trapping in intermediate phases and minimising local electric fields that drive ion migration and halide segregation. Efficient, spectrally well-defined funnelling, characterised by rapid low-*n* to high-*n* energy transfer serves as a hallmark of low defect density, robust organic inorganic interfaces, and controlled lattice strain. This interplay is clearly reflected in additive-engineered quasi-2D PeLEDs, where molecular additives simultaneously tailor the n-phase distribution and passivate defects, resulting in higher external quantum efficiency and markedly extended device lifetimes.[139] By rapidly directing excitons into lower-energy radiative domains, efficient funnelling reduces exciton residence near defect-rich regions, suppressing nonradiative recombination and mitigating photo-induced ionic motion. Conversely, inefficient funnelling leads to exciton bottlenecks, localised heating, and high carrier densities, which promote halide segregation, ligand loss, and lattice distortion in structurally vulnerable regions. Overall, these advances underscore the importance of strategic spacer cation design and a detailed understanding of interfacial and energy-transfer dynamics in achieving stable, high-performance perovskite optoelectronic devices.[4,140] (see Table 1 for a summary of A-site cations and their applications).

8. Computational perspectives on charge and energy transport in LD/3D perovskite heterojunctions

8.1. Interfacial band alignment and ultrafast carrier dynamics

Although perovskite devices have demonstrated remarkable efficiencies exceeding 26%, a comprehensive theoretical understanding of the fundamental mechanisms, which is crucial for the rational design of these heterojunctions, is lacking. Their unique confinement effects and synergistic transfer pathways for charge, excitons, and phonons are difficult to capture experimentally. Simulations help elucidate band alignment, defect dynamics, and interfacial energetics, offering critical insights into the design principles governing performance in perovskite-based optoelectronic devices. DFT[26] and its advanced extensions, such as GW, non-adiabatic molecular dynamics (NAMD), have played a pivotal role in probing the electronic structures (Fig. 7(a)–(f)) and intricate interactions at these heterojunctions and deciphering the atomistic and electronic origins of various phenomena.[141] This section focuses on the computational and theoretical perspective of understanding the fundamental processes governing the energy and charge transfer in LD/3D perovskite heterojunctions, emphasising interfacial band-alignment and heterojunction formation, exciton dissociation and charge carrier dynamics, phonon-assisted energy funnelling and TET, defect tolerance, and interfacial stability.

The electronic coupling between LD and 3D perovskite phases is primarily determined by the relative band alignment, which can be of Type-I (straddling) or Type-II (staggered), dictating the flow of charges and energy. DFT simulations are instrumental in elucidating these alignments. Recent

Table 1 Summary of A-site cations in perovskites with their functions and applications

A site cation	Type	Applications in perovskites	Functions
Methylammonium (MA^+, $CH_3NH_3^+$)[125]	Alkyl (short-chain)	3D, solar cells, LEDs	Forms 3D; decent efficiency but limited thermal stability
Formamidinium (FA^+, $HC(NH_2)_2^+$)[124]	Alkyl (short-chain, pseudo-aromatic resonance)	3D, solar cells, LEDs	Improves thermal stability; favours black α-phase in $FAPbI_3$
Cesium (Cs^+) (inorganic but often mixed)[107]	—	Solar cells, LEDs, tandem devices (3D and quasi 2D)	Improves stability when alloyed with MA/FA
Butylammonium (BA^+, $C_4H_9NH_3^+$)[65]	Alkyl (linear)	2D/3D perovskite solar cells, LEDs	Spacer cation; enhances stability and moisture resistance
IBA (iso-butylammonium)[124]	Alkyl	2D/3D perovskite solar cells	Stabilises α phase of $FAPbI_3$, excellent operational efficiency and stability
Octylammonium (OA^+, $C_8H_{17}NH_3^+$)[126]	Alkyl (long-chain)	2D/3D LEDs, passivation layers	Improves moisture stability; often used in quasi-2D LEDs
4-*tert*-Butyl-benzylammonium iodide (*t*BBAI)[13]	Aryl–alkyl hybrid	Perovskite solar cells	Accelerates the charge extraction from the perovskite into the hole-transporter, retarding nonradiative charge carrier recombination
Phenethylammonium (PEA^+, $C_6H_5–CH_2–CH_2–NH_3^+$)[66]	Aryl	2D/3D PeLEDs, solar cells	Widely used for layered perovskites; improves phase stability and EL, energy funneling
Pentafluorophenylethylammonium (FEA)[21] *p*-fluorophenethylammonium[112]	Aryl	2D/3D perovskite solar cells, quasi-2D PeLEDs	Excellent performance and stability over 1000 hours; bright PeLED
Naphthylmethylammonium (NMA^+)[127]	Aryl (extended)	2D perovskite LEDs, solar cells	Strong π–π interactions; enhances exciton confinement
Thiophene-based ammoniums (*e.g.*, $ThMA^+$)-MeBThMAI and CNBThMAI[75]	Aryl	LEDs, photodetectors	Improves charge transport *via* conjugated backbone, energy transport
Methylhydrazinium (MHy^+, $CH_3NH_2NH_2^+$)[128–130]	Alkyl (short-chain, non-linear, asymmetric)	Wide bandgap perovskite solar cells	Suppresses iodide oxidation and halide demixing
Imidazolium cations like-(*N*,*N*′-dialkylbenzimidazolium iodide)[131] 1-Butyl-3-methylimidazolium iodide (BMI),[132] 1-ethyl-3-methylimidazolium tetrafluoroborate ($EMIMBF_4$)[133]	Cyclic (one-dimensional single-chain structure)	1D capping layer topped 1D/3D structure; quasi-2D-PeLEDs and solar cells	Defect passivation interface improvement, enhances stability

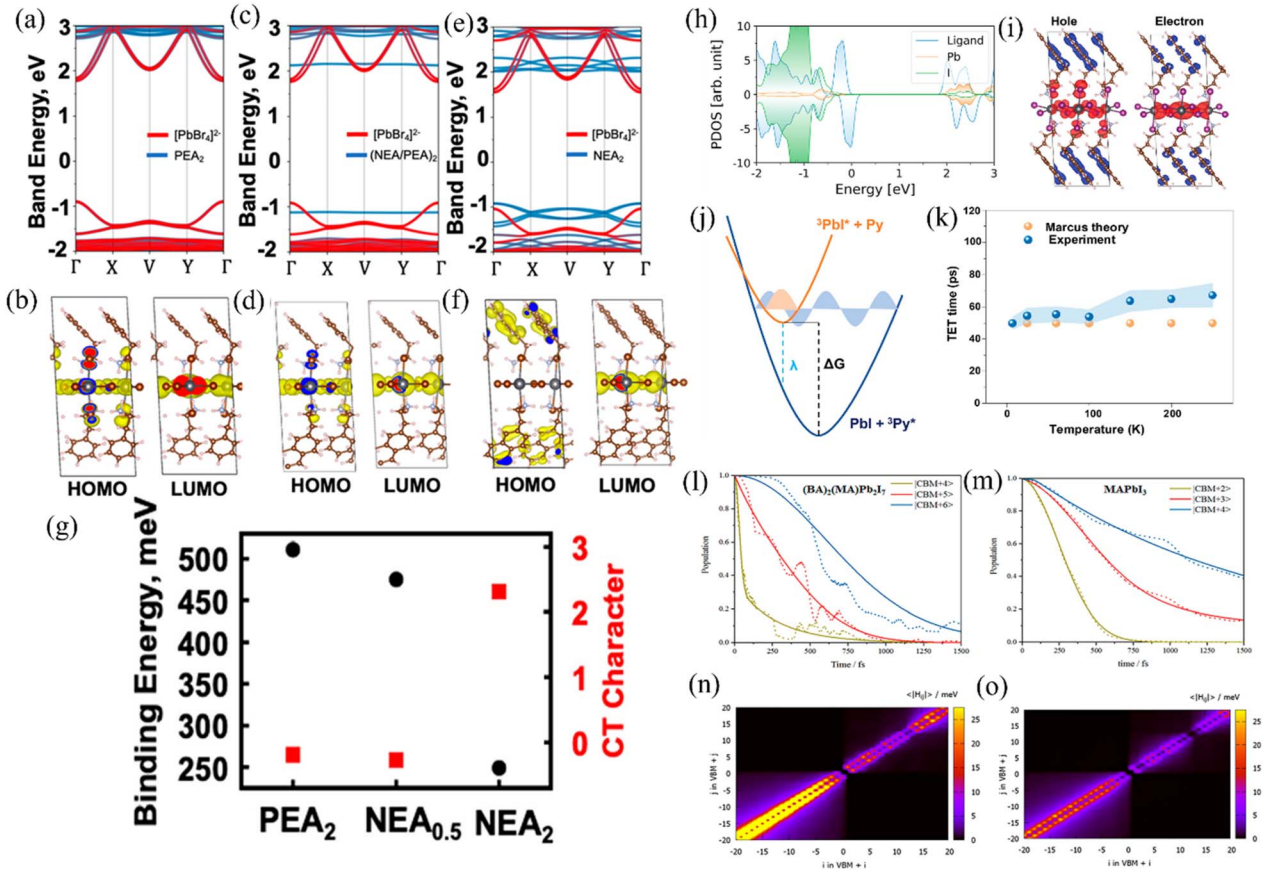

Fig. 7 Simulated electronic structure considering the HOMO and LUMO Kohn–Sham orbitals at the high-symmetry point for (a) and (b) PEA_2PbBr_4, (c) and (d) $PEA_{1.50}NEA_{0.50}PbBr_4$, and (e) and (f) NEA_2PbBr_4. The red and blue curves represent the projected atomic contributions from the lead octahedra and organic moiety. (g) Estimated exciton binding energy (left axis, black circles) and charge-transfer (CT) character (right axis, red squares) for the lowest-energy exciton across this class of 2D perovskites.[141] Quantum-tunnelling-driven TET. (h) Spin-polarised projected density of states (PDOS) for the $(PyBA)_2PbI_4$ system, with the charge densities of the initial TET orbitals localised in the lead-iodide layer. (i) Charge density difference between the final and initial orbitals of the hole (left) and the electron (right) involved in TET. Red indicates the initial orbitals localised onto the $[PbI_4]^{2-}$ perovskite core, while blue indicates the final orbitals localised onto the pyrene molecular layer. (j) Schematic representation of the Gibbs free energy surfaces as a function of the nuclear configuration of TET from Pb–I to pyrene in the Marcus-inverted regime, illustrating the enhanced vibrational overlap between the donor and acceptor wave functions. (k) Plot showing the theoretically predicted (orange) and experimentally determined (blue) TET time scales as a function of temperature, demonstrating the weak T-dependence of the triplet transfer rate due to tunneling. The shaded blue area indicates the experimental uncertainties in determining the TET times[68] (reproduced from ref. 68 with permission from American Chemical Society, copyright 2024). Fitted time evolution of populations for hot electrons and average nonadiabatic couplings (NAC) between all related electronic states during the NAMD simulations for $(BA)_2(MA)Pb_2I_7$ (l and n) and $MAPbI_3$ (m and o)[157] (reproduced from ref. 157 with permission from American Chemical Society, copyright 2019).

experimental and computational studies have demonstrated the tuning of the effective bandgap by modulating the interfacial charge transfer in model 2D/3D interfaces.[57,142,143] Recent high-throughput DFT screening, accelerated by machine learning algorithms, has identified optimal organic spacer cations that can fine-tune the band offsets while maintaining structural stability.[144,145] The introduction of π-conjugated spacers can enhance charge delocalisation across the heterointerface, as is evidenced by projected density of states (PDOS) analyses.

Electron–phonon interactions at the LD/3D interfaces can either suppress traps and aid transport or enhance recombination,[18,146] depending on material properties. Thus, understanding phonon-driven charge dynamics is crucial for optimising device performance. The actual charge separation at these interfaces occurs on ultrafast timescales, as is revealed by NAMD simulations.[147,148] These studies demonstrate that the initial photoexcitation in the LD phase rapidly dissociates at the interface, with electrons injected into the 3D phase within hundreds of femtoseconds.[149] The organic spacer layer between the perovskite sheets is crucially responsible for the modulation of these processes.[150,151] Kinetic Monte-Carlo simulations further complement these findings by modelling defect-assisted trapping and detrapping processes, showing that the passivated interfaces exhibit carrier diffusion lengths of greater than 1 μm.[152]

8.2. Exciton dissociation and energy transfer pathways

While 3D perovskites naturally dissociate excitons due to low binding energies, 2D perovskites—despite strong exciton binding—also yield free carriers under illumination, likely *via*

edge states or polaron screening.[14,153] Exciton dissociation in Type-II band alignment is mediated through interfacial charge transfer. The 2D component acts as the exciton harvester, while the 3D phase provides efficient charge transport channels. The computational insights from time-dependent (TD) DFT and NAMD reveal ultrafast electron transfer from 2D to 3D domains with vibronic coupling as the leading force of exciton decoherence.[147] The emerging paradigm suggests two synergistic pathways: direct exciton dissociation into free carriers at the interface and energy funnelling to the 3D phase, which is governed by band alignment and interfacial fields.

Besides charge separation, energy transfer processes in LD/3D perovskite heterojunctions play a pivotal role in optoelectronic functionality, especially in light-emitting devices. A well-established energy transfer mechanism, FRET, can funnel excitonic energy from a 2D donor to a 3D acceptor if the emission spectrum of 2D overlaps with the absorption spectrum of 3D. Computationally, one can evaluate the FRET rates by calculating exciton wavefunctions and dipole moments *via* time-dependent DFT, confirming that the oriented 2D/3D crystals with small spacing yield enhanced FRET efficiency.[89,154] For tightly coupled interfaces, Dexter energy transfer may also occur.[68] Dexter mechanism requires wavefunction overlap and can lead to energy transfer, including spin-forbidden excitons. Pure Dexter transfer is less common amongst the inorganic perovskite layers but becomes relevant in cases where triplet states are involved or when an exciton is deeply trapped in a 2D layer and is unable to dissociate. TET is important while considering perovskite heterojunctions with organic components. Due to strong SOC effects for lead and heavy halides, intersystem crossing can populate the triplet excitons either in perovskite layers or adjacent organic spacers.[68,155,156] For example, in a 2D perovskite with an aromatic spacer (like naphthylethylammonium, NEA), it was shown that upon excitation, the hole localises on the organic moiety while the electron remains in the Pb–I framework, effectively creating an excited triplet on the organic part.[104,141] Theoretical modelling of these processes involves calculating the electronic coupling for triplet states and can leverage DFT/Marcus theory or multireference methods, since an accurate description of spin-triplet energetics is required.[68,69,155] TD-DFT and NAMD simulations are essential for understanding the charge transport and energy transfer processes, as summarised in Fig. 7(g)–(o). They also help in investigating the impact of strain and defects on the long-term stability and charge transport efficiency of the device. Theoretical models such as FRET and DET are useful for studying the energy transfer between excitons at the LD/3D interface. FRET typically occurs over long distances, while DET is effective for short-range interactions. TET is particularly important when triplet excitons are involved. These models help in understanding how energy is transferred across the interface and the efficiency of charge separation and extraction.

LD/3D perovskite heterojunctions can redirect excitation energy through FRET or Dexter/TET pathways in addition to direct charge transfer. These mechanisms have practical consequences, such as FRET-based exciton funnelling in quasi-2D perovskites enhances the radiative efficiencies in LEDs by concentrating excitations in the lowest bandgap domains, while TET opens pathways for multi-layer upconversion and hybrid spintronic devices. Computational studies that simulate excitonic states and their couplings provide quantitative estimates of FRET rates and Dexter exchange integrals, linking molecular-level interactions to experimentally observed energy transfer dynamics.[68,158] The ability to harness the synergy between energy and charge transfer in these systems makes these perovskite heterojunctions quite promising for next-generation optoelectronics.

9. Outlook and conclusive remarks

A significant research gap remains in understanding the complex interplay of energy and charge transfer in LD/3D perovskite heterojunctions, an area crucial for advancing perovskite-based optoelectronic devices. While charge-transfer mechanisms have been partially explored, the role of energy transfer and its correlation with charge dynamics are still not well established. Band alignment at the LD/3D interface, which is strongly influenced by the size and type of organic cations, requires thorough investigation to enable precise control of carrier dynamics for targeted applications.

LD perovskites are known to offer superior environmental and photostability compared to their 3D counterparts; however, processes such as defect passivation and interfacial charge transfer remain insufficiently studied. In addition, mechanisms such as Dexter and Förster resonance energy transfer are not yet fully understood, and the dominant pathway at the LD/3D interface is still debated. Although incorporating LD layers onto 3D perovskites can enhance device stability, this often comes at the cost of reduced performance due to lattice mismatch and misaligned energy levels. Addressing these challenges requires a comprehensive framework that examines junction potential, charge distribution, and excitonic behaviour under varying bias conditions. Interface engineering in LD/3D systems is therefore critical to balancing excitonic and free-carrier processes. By tailoring factors such as layer orientation, interfacial quality, and dipole alignment, it is possible to optimise both energy and charge transport, paving the way for stable, high-performance perovskite optoelectronics. Bridging the knowledge gap between charge and energy transfer will demand not only systematic experimental validation but also predictive theoretical modelling. Key aspects include excitonic processes, triplet energy transfer, and interface-induced charge dynamics. The influence of parameters such as organic cation size and type, dielectric and quantum confinement, exciton binding energy, and recombination dynamics must be carefully evaluated. While 2D perovskites are well reported for their role in defect passivation and stability, the fundamental understanding of their relatively low photoluminescence quantum efficiency remains underexplored. In particular, perovskites incorporating conjugated organic cations present exciting opportunities, with simulations already indicating their potential—yet experimental studies in optoelectronic devices are still limited.

Finally, the design requirements differ by application: for LEDs, stronger exciton confinement is desirable to boost radiative recombination, whereas for solar cells, efficient charge separation and extraction are paramount. A deeper understanding of these contrasting requirements will be key to tailoring LD/3D heterojunctions for diverse optoelectronic platforms.

Author contributions

Bidisha Nath: investigation, writing – original draft (lead), review and editing. Pradhi Srivastava: writing – original draft (supporting). Junjie Xie: writing – original draft (supporting). Tajamul A. Wani: writing – original draft (supporting). Karima Al-Hawiti: writing – original draft (supporting). Xiaohan Jia: writing – original draft (supporting), Neha Arora: writing – original draft (supporting), M. Ibrahim Dar: conceptualisation, investigation, writing – original draft (lead), review and editing, supervision and funding acquisition.

Conflicts of interest

There are no conflicts to declare.

Data availability

No primary research results, software or code have been included and no new data were generated or analysed as part of this review.

Acknowledgements

Authors acknowledge support from the Royal Society.

Notes and references

1 Y. Han, S. Yue and B. Bin Cui, *Adv. Sci.*, 2021, **8**, 2004805.
2 C. Ma, D. Shen, B. Huang, X. Li, W. C. Chen, M. F. Lo, P. Wang, M. Hon-Wah Lam, Y. Lu, B. Ma and C. S. Lee, *J. Mater. Chem. A*, 2019, **7**, 8811–8817.
3 F. Wang, Y. Sun, T. Wang, X. Sun, G. Yang, Y. Li, Q. Li, X. Liang, X. Zhou, J. Lv, Q. Zhu, C. Yang, H. Lin, M. Yuan, G. Li and H. Hu, *Nano Energy*, 2024, **129**, 110063.
4 Y. Miao, Y. Chen, H. Chen, X. Wang and Y. Zhao, *Chem. Sci.*, 2021, **12**, 7231–7247.
5 N. N. Som, P. M. W. P. Sampath, S. D. Dabhi, V. Mankad, S. Shinde, M. L. C. Attygalle and P. K. Jha, *Sol. Energy*, 2018, **173**, 1315–1322.
6 D. B. Mitzi, *J. Chem. Soc., Dalton Trans.*, 2001, **1**, 1–12.
7 Y. Zhang, M. Abdi-Jalebi, B. W. Larson and F. Zhang, *Adv. Mater.*, 2024, **36**, 2404517.
8 S. Sun, M. Lu, X. Gao, Z. Shi, X. Bai, W. W. Yu and Y. Zhang, *Adv. Sci.*, 2021, **8**, 2102689.
9 Z. Yuan, C. Zhou, Y. Tian, Y. Shu, J. Messier, J. C. Wang, L. J. Van De Burgt, K. Kountouriotis, Y. Xin, E. Holt, K. Schanze, R. Clark, T. Siegrist and B. Ma, *Nat. Commun.*, 2017, **8**, 1–7.
10 W. Deng, L. Huang, X. Xu, X. Zhang, X. Jin, S. T. Lee and J. Jie, *Nano Lett.*, 2017, **17**, 2482–2489.
11 D. Duan, C. Ge, M. Z. Rahaman, C. H. Lin, Y. Shi, H. Lin, H. Hu and T. Wu, *NPG Asia Mater.*, 2023, **15**(1), 1–22.
12 X. Li, S. Aftab, S. Hussain, F. Kabir, A. M. A. Henaish, A. G. Al-Sehemi, M. R. Pallavolu and G. Koyyada, *J. Mater. Chem. A*, 2024, **12**, 4421–4440.
13 H. Zhu, Y. Liu, F. T. Eickemeyer, L. Pan, D. Ren, M. A. Ruiz-Preciado, B. Carlsen, B. Yang, X. Dong, Z. Wang, H. Liu, S. Wang, S. M. Zakeeruddin, A. Hagfeldt, M. I. Dar, X. Li and M. Grätzel, *Adv. Mater.*, 2020, **32**, 1907757.
14 J.-C. Blancon, H. Tsai, W. Nie, C. C. Stoumpos, L. Pedesseau, C. Katan, M. Kepenekian, C. M. M. Soe, K. Appavoo, M. Y. Sfeir, S. Tretiak, P. M. Ajayan, M. G. Kanatzidis, J. Even, J. J. Crochet and A. D. Mohite, *Science*, 2017, **355**, 1288–1292.
15 Y. Jiang, J. Wei and M. Yuan, *J. Phys. Chem. Lett.*, 2021, **12**(10), 2593–2606.
16 B. Saparov and D. B. Mitzi, *Chem. Rev.*, 2016, **116**, 4558–4596.
17 D. Marongiu, M. Saba, F. Quochi, A. Mura and G. Bongiovanni, *J. Mater. Chem. C*, 2019, **7**, 12006–12018.
18 A. Mahata, E. Mosconi, D. Meggiolaro, S. Fantacci and F. De Angelis, *Adv. Energy Mater.*, 2023, **15**, 2303405.
19 K. Ma, J. Sun and L. Dou, *Chem. Commun.*, 2024, **60**, 7824–7842.
20 M. Abdi-Jalebi, M. I. Dar, S. P. Senanayak, A. Sadhanala, Z. Andaji-Garmaroudi, L. M. Pazos-Outón, J. M. Richter, A. J. Pearson, H. Sirringhaus, M. Grätzel and R. H. Friend, *Sci. Adv.*, 2019, **5**, eaav2012.
21 Y. Liu, S. Akin, L. Pan, R. Uchida, N. Arora, J. V. Milić, A. Hinderhofer, F. Schreiber, A. R. Uhl, S. M. Zakeeruddin, A. Hagfeldt, M. I. Dar and M. Grätzel, *Sci. Adv.*, 2019, **5**, eaaw2543.
22 G. Uzurano, N. Kuwahara, T. Saito, A. Fujii and M. Ozaki, *ACS Mater. Lett.*, 2022, **4**, 378–384.
23 J. W. Lee, S. Tan, T. H. Han, R. Wang, L. Zhang, C. Park, M. Yoon, C. Choi, M. Xu, M. E. Liao, S. J. Lee, S. Nuryyeva, C. Zhu, K. Huynh, M. S. Goorsky, Y. Huang, X. Pan and Y. Yang, *Nat. Commun.*, 2020, **11**, 5514.
24 M. S. de Holanda, R. Szostak, P. E. Marchezi, L. G. T. A. Duarte, J. C. Germino, T. D. Z. Atvars and A. F. Nogueira, *Sol. RRL*, 2019, **3**, 1900199.
25 L. Zhao, P. Tang, D. Luo, M. Ibrahim Dar, F. T. Eickemeyer, N. Arora, Q. Hu, J. Luo, Y. Liu, S. Mohammed Zakeeruddin, A. Hagfeldt, J. Arbiol, W. Huang, Q. Gong, T. P. Russell, R. H. Friend, M. Grätzel and R. Zhu, *Sci. Adv.*, 2022, **8**, 3733.
26 A. H. Proppe, A. Johnston, S. Teale, A. Mahata, R. Quintero-Bermudez, E. H. Jung, L. Grater, T. Cui, T. Filleter, C. Y. Kim, S. O. Kelley, F. De Angelis and E. H. Sargent, *Nat. Commun.*, 2021, **12**, 3472.
27 M. Pazoki, R. Imani, A. Röckert and T. Edvinsson, *J. Mater. Chem. A*, 2022, **10**, 20896–20904.
28 X. Li, W. Ke, B. Traoré, P. Guo, I. Hadar, M. Kepenekian, J. Even, C. Katan, C. C. Stoumpos, R. D. Schaller and M. G. Kanatzidis, *J. Am. Chem. Soc.*, 2019, **141**, 12880–12890.

29 W. T. M. Van Gompel, L. Lutsen and D. Vanderzande, *J. Mater. Chem. C*, 2023, **11**, 12877–12893.
30 G. Kakavelakis, M. Gedda, A. Panagiotopoulos, E. Kymakis, T. D. Anthopoulos and K. Petridis, *Adv. Sci.*, 2020, **7**, 2002098.
31 T. L. Leung, I. Ahmad, A. A. Syed, A. M. C. Ng, J. Popović and A. B. Djurišić, *Commun. Mater.*, 2022, **3**(1), 1–10.
32 T. Baumeler, A. A. Saleh, T. A. Wani, S. Huang, X. Jia, X. Bai, M. Abdi-Jalebi, N. Arora, M. Grätzel and M. I. Dar, *ACS Mater. Lett.*, 2023, **5**, 2408–2421.
33 T. A. Wani, J. Shamsi, X. Bai, N. Arora and M. I. Dar, *ACS Omega*, 2023, **8**, 17337–17349.
34 L. Scalon, C. A. Nogueira, A. F. V. Fonseca, P. E. Marchezi, R. F. Moral, G. Grancini, T. Kodalle, C. M. Sutter-Fella, C. C. Oliveira, L. F. Zagonel and A. F. Nogueira, *ACS Appl. Mater. Interfaces*, 2024, **16**, 51727–51737.
35 M. Xiong, W. Zou, K. Fan, C. Qin, S. Li, L. Fei, J. Jiang, H. Huang, L. Shen, F. Gao, A. K. Y. Jen and K. Yao, *ACS Energy Lett.*, 2022, **7**, 550–559.
36 H. Wang, C. Zhu, L. Liu, S. Ma, P. Liu, J. Wu, C. Shi, Q. Du, Y. Hao, S. Xiang, H. Chen, P. Chen, Y. Bai, H. Zhou, Y. Li and Q. Chen, *Adv. Mater.*, 2019, **31**, 1904408.
37 M. L. Kepenekian, B. Traore, J.-C. Blancon, L. Pedesseau, H. Tsai, W. Nie, C. C. Stoumpos, M. G. Kanatzidis, J. Even, A. D. Mohite, S. Tretiak and C. Katan, *Nano Lett.*, 2018, **18**, 53.
38 Y. Zou, Y. Cui, H. Y. Wang, Q. Cai, C. Mu and J. P. Zhang, *Nanotechnology*, 2019, **30**, 275202.
39 Z. Wang, X. Duan, J. Zhang, W. Yuan, D. Qu, Y. Chen, L. He, H. Wang, G. Yang, W. Zhang, Y. Bai and H. M. Cheng, *Commun. Mater.*, 2024, **5**(1), 1–18.
40 P. Li, C. Liang, X.-L. Liu, F. Li, Y. Zhang, X.-T. Liu, H. Gu, X. Hu, G. Xing, X. Tao and Y. Song, *Adv. Mater.*, 2019, **31**, 1901966.
41 Y. Hu, L. M. Spies, D. Alonso-Álvarez, P. Mocherla, H. Jones, J. Hanisch, T. Bein, P. R. F. Barnes and P. Docampo, *J. Mater. Chem. A*, 2018, **6**, 22215–22225.
42 B. P. Nguyen, J. Kim, H. K. Park, W. Jo and G. Y. Kim, *ACS Appl. Energy Mater.*, 2022, **5**, 7965–7976.
43 D. Lin, J. Fang, S. Li, Z. Zhan, H. Li, X. Wang, G. Xie, D. Wang, N. Huang, H. Peng, W. Xie, L. K. Ono, Y. Qi and L. Qiu, *Adv. Sci.*, 2025, **12**, 2407380.
44 J. Nie, Y. Zhang, J. Wang, L. Li and Y. Zhang, *ACS Energy Lett.*, 2024, **9**, 1674–1681.
45 P. Liu, X. Li, T. Cai, W. Xing, N. Yang, H. Arandiyan, Z. Shao, S. Wang and S. Liu, *Nano-Micro Lett.*, 2024, **17**(1), 1–44.
46 Z. Sunli, Y. Liu, S. Li, J. Ren, Y. Wu, Q. Sun, Y. Cui, M. Chen and Y. Hao, *ACS Appl. Mater. Interfaces*, 2022, **14**, 7417–7427.
47 T. He, S. Li, Y. Jiang, C. Qin, M. Cui, L. Qiao, H. Xu, J. Yang, R. Long, H. Wang and M. Yuan, *Nat. Commun.*, 2020, **11**, 1–11.
48 P. Kumar, A. Satinder, K. Sharma and R. Singh, *EES Sol.*, 2025, **1**, 356–365.
49 L. Hu, H. Li, B. Xu, Y. Liu, P. Yang, X. Gao, P. Li, J. Wang and R. Li, *ACS Appl. Mater. Interfaces*, 2024, **16**, 42221–42229.
50 T. Umebayashi, K. Asai, T. Kondo and A. Nakao, *Phys. Rev. B*, 2003, **67**, 155405.
51 E. I. Marchenko, V. V. Korolev, A. Mitrofanov, S. A. Fateev, E. A. Goodilin and A. B. Tarasov, *Chem. Mater.*, 2021, **33**, 1213–1217.
52 E. I. Marchenko, V. V. Korolev, S. A. Fateev, A. Mitrofanov, N. N. Eremin, E. A. Goodilin and A. B. Tarasov, *Chem. Mater.*, 2021, **33**, 7518–7526.
53 P. Liu, S. Yu and S. Xiao, *Sustainable Energy Fuels*, 2021, **5**, 3950–3978.
54 D. Yu, F. Cao, C. Su and G. Xing, *Acc. Chem. Res.*, 2023, **56**, 959–970.
55 L. Zhang, X. Zhang and G. Lu, *J. Phys. Chem. Lett.*, 2020, **11**, 2910–2916.
56 M. Feng, L. Kong, J. Chen, H. Ma, C. Zha and L. Zhang, *J. Chem. Phys.*, 2024, **161**, 24703.
57 M. Y. Kuo, N. Spitha, M. P. Hautzinger, P. L. Hsieh, J. Li, D. Pan, Y. Zhao, L. J. Chen, M. H. Huang, S. Jin, Y. J. Hsu and J. C. Wright, *J. Am. Chem. Soc.*, 2021, **143**, 4969–4978.
58 A. Mahata, E. Mosconi, D. Meggiolaro and F. De Angelis, *Chem. Mater.*, 2020, **32**, 105–113.
59 P. Basera, B. Traoré, J. Even and C. Katan, *J. Mater. Chem. A*, 2023, **15**, 11884.
60 S. Sun, T. Salim, N. Mathews, M. Duchamp, C. Boothroyd, G. Xing, T. C. Sum and Y. M. Lam, *Energy Environ. Sci.*, 2014, **7**, 399–407.
61 T. H. Főrster, *Discuss. Faraday Soc.*, 1959, **27**, 7–17.
62 S. Bai, P. Zhang and D. N. Beratan, *J. Phys. Chem. C*, 2020, **124**, 18956–18960.
63 P. Chen, Y. Meng, M. Ahmadi, Q. Peng, C. Gao, L. Xu, M. Shao, Z. Xiong and B. Hu, *Nano Energy*, 2018, **50**, 615–622.
64 S. Panuganti, L. V. Besteiro, E. S. Vasileiadou, J. M. Hoffman, A. O. Govorov, S. K. Gray, M. G. Kanatzidis and R. D. Schaller, *J. Am. Chem. Soc.*, 2021, **143**, 4244–4252.
65 H. Esmaielpour, V. R. Whiteside, S. Sourabh, G. E. Eperon, J. T. Precht, M. C. Beard, H. Lu, B. K. Durant and I. R. Sellers, *J. Phys. Chem. C*, 2020, **124**, 9496–9505.
66 S. Neutzner, F. Thouin, D. Cortecchia, A. Petrozza, C. Silva, A. Ram and S. Kandada, *Phys. Rev. Mater.*, 2018, **2**, 64605.
67 K. Ema, M. Inomata, Y. Kato, H. Kunugita and M. Era, *Phys. Rev. Lett.*, 2008, **100**, 257401.
68 A. De, C. Mora Perez, A. Liang, K. Wang, L. Dou, O. Prezhdo and L. Huang, *J. Am. Chem. Soc.*, 2024, **146**, 4260–4269.
69 X. Luo, R. Lai, Y. Li, Y. Han, G. Liang, X. Liu, T. Ding, J. Wang and K. Wu, *J. Am. Chem. Soc.*, 2019, **141**, 4186–4190.
70 E. D. Kinigstein, H. Tsai, W. Nie, J. C. Blancon, K. G. Yager, K. Appavoo, J. Even, M. G. Kanatzidis, A. D. Mohite and M. Y. Sfeir, *ACS Mater. Lett.*, 2020, **2**, 1360–1367.
71 F. Zhang, B. Cai, J. Song, B. Han, B. Zhang and H. Zeng, *Adv. Funct. Mater.*, 2020, **30**, 2001732.
72 L. N. Quan, Y. Zhao, F. P. García De Arquer, R. Sabatini, G. Walters, O. Voznyy, R. Comin, Y. Li, J. Z. Fan, H. Tan, J. Pan, M. Yuan, O. M. Bakr, Z. Lu, D. H. Kim and E. H. Sargent, *Nano Lett.*, 2017, **17**, 3701–3709.

73 Y. Fu, W. Zheng, X. Wang, M. P. Hautzinger, D. Pan, L. Dang, J. C. Wright, A. Pan and S. Jin, *J. Am. Chem. Soc.*, 2018, **140**, 15675–15683.
74 S. Ramakrishnan, H. Li, Y. Xu, D. Shin, I. Dursun, M. Cotlet, Y. Zhang and Q. Yu, *Sol. RRL*, 2022, **6**, 2200490.
75 X. Dong, H. Zhang, J. Li, L. Yang, Y. Ma, H. Liu, Z. Hu and Y. Liu, *Angew. Chem., Int. Ed.*, 2025, **64**, e202501210.
76 R. Chakraborty, G. Paul and A. J. Pal, *Phys. Rev. Appl.*, 2022, **17**, 54045.
77 S. Kumar, J. Jagielski, S. Yakunin, P. Rice, Y. C. Chiu, M. Wang, G. Nedelcu, Y. Kim, S. Lin, E. J. G. Santos, M. V. Kovalenko and C. J. Shih, *ACS Nano*, 2016, **10**, 9720–9729.
78 S. D. Baek, S. J. Yang, H. Yang, W. Shao, Y. T. Yang and L. Dou, *Adv. Mater.*, 2024, **37**, 2411998.
79 Z. He, C. Peng, R. Guo, B. Chen, F. Zhang, X. He, X. Zhu, Y. Xiong, J. Chen, W. Liang and L. Wang, *Chem. Eng. J.*, 2025, **505**, 159894.
80 P. Caprioglio, J. A. Smith, R. D. J. Oliver, A. Dasgupta, S. Choudhary, M. D. Farrar, A. J. Ramadan, Y. H. Lin, M. G. Christoforo, J. M. Ball, J. Diekmann, J. Thiesbrummel, K. A. Zaininger, X. Shen, M. B. Johnston, D. Neher, M. Stolterfoht and H. J. Snaith, *Nat. Commun.*, 2023, **14**, 932.
81 B. Singh, N. G. Saykar, B. S. Kumar, D. Afria, C. K. Sangeetha and S. R. Rondiya, *ACS Omega*, 2024, **9**(9), 10000–10016.
82 P. C. Huang, S. K. Huang, T. C. Lai, M. C. Shih, H. C. Hsu, C. H. Chen, C. C. Lin, C. H. Chiang, C. Y. Lin, K. Tsukagoshi, C. W. Chen, Y. P. Chiu, S. F. Tsay and Y. C. Wang, *Nano Energy*, 2021, **89**, 106362.
83 B. Li, Q. Liu, J. Gong, S. Li, C. Zhang, D. Gao, Z. Chen, Z. Li, X. Wu, D. Zhao, Z. Yu, X. Li, Y. Wang, H. Lu, X. C. Zeng and Z. Zhu, *Nat. Commun.*, 2024, **15**, 1–9.
84 X. Chang, R. Azmi, T. Yang, N. Wu, S. Y. Jeong, H. Xi, D. Satrio Utomo, B. Vishal, F. H. Isikgor, H. Faber, Z. Ling, M. He, M. Marengo, P. Dally, A. Prasetio, Y. Y. Yang, C. Xiao, H. Y. Woo, K. Zhao, M. Heeney, S. De Wolf, L. Tsetseris and T. D. Anthopoulos, *Nat. Commun.*, 2025, **16**, 1–10.
85 C. Li, J. Yang, F. Su, J. Tan, Y. Luo and S. Ye, *Nat. Commun.*, 2020, **11**, 1–8.
86 G. Grancini and M. K. Nazeeruddin, *Nat. Rev. Mater.*, 2019, **4**, 4–22.
87 M. C. Gélvez-Rueda, E. M. Hutter, D. H. Cao, N. Renaud, C. C. Stoumpos, J. T. Hupp, T. J. Savenije, M. G. Kanatzidis and F. C. Grozema, *J. Phys. Chem. C*, 2017, **121**, 26566–26574.
88 I. Metcalf, S. Sidhik, H. Zhang, A. Agrawal, J. Persaud, J. Hou, J. Even and A. D. Mohite, *Chem. Rev.*, 2023, **123**, 9565–9652.
89 X. Zhang, J. Zhou, F. Zheng, B. Yang, A. Jha and H. G. Duan, *Commun. Phys.*, 2025, **8**, 71.
90 K. Wei, T. Jiang, Z. Xu, J. Zhou, J. You, Y. Tang, H. Li, R. Chen, X. Zheng, S. Wang, K. Yin, Z. Wang, J. Wang, X. Cheng, K. Wei, T. Jiang, Z. Xu, J. Zhou, Y. Tang, H. Li, X. Cheng, J. You, X. Zheng, K. Yin, Z. Wang, R. Chen, S. Wang and J. Wang, *Laser Photonics Rev.*, 2018, **12**, 1800128.
91 R. L. Milot, R. J. Sutton, G. E. Eperon, A. A. Haghighirad, J. Martinez Hardigree, L. Miranda, H. J. Snaith, M. B. Johnston and L. M. Herz, *Nano Lett.*, 2016, **16**, 7001–7007.
92 F. Faini, Y. Asensio, F. Visentin, L. Olano-Vegas, M. Hörmann, L. E. Hueso, G. Cerullo, F. V. A. Camargo, B. Martín-García and G. Grancini, *ACS Energy Lett.*, 2024, **13**, 120–127.
93 H. Pang, S. Du, J. Deng, W. Kong, Y. Zhao, B. Zheng and L. Ma, *Small*, 2024, **20**, 2401797.
94 D. Yu, F. Cao, J. Liao, B. Wang, C. Su and G. Xing, *Nat. Commun.*, 2022, **13**, 6229.
95 J. Even, L. Pedesseau, J. M. Jancu and C. Katan, *J. Phys. Chem. Lett.*, 2013, **4**, 2999–3005.
96 J. J. Yang, W. K. Chen, X. Y. Liu, W. H. Fang and G. Cui, *JACS Au*, 2021, **1**, 1178–1186.
97 W. Li, L. Zhou, O. V. Prezhdo and A. V. Akimov, *ACS Energy Lett.*, 2018, **3**, 2159–2166.
98 Y. Zhang, Y. Zhang, B. Niu, Y. Huang, H. Wu, W. Fu and H. Chen, *Adv. Funct. Mater.*, 2023, **33**, 2307949.
99 M. Lee, J. Lim, E. Choi, A. M. Soufiani, S. Lee, F. J. Ma, S. Lim, J. Seidel, D. H. Seo, J. S. Park, W. Lee, J. Lim, R. F. Webster, J. Kim, D. Wang, M. A. Green, D. Kim, J. H. Noh, X. Hao and J. S. Yun, *Adv. Mater.*, 2024, **36**, 2402053.
100 J. Fan, Y. Ma, C. Zhang, C. Liu, W. Li, R. E. I Schropp, Y. Mai, J. Fan, C. Liu, W. Li, Y. Mai, Y. Ma, C. Zhang and R. E. I Schropp, *Adv. Energy Mater.*, 2018, **8**, 1703421.
101 Z. Yang, J. Cui, Y. Sun, J. Yao, S. Yang and J. Song, *Nat. Commun.*, 2025, **16**, 6909.
102 D. Cortecchia, J. Yin, A. Bruno, S. Z. A. Lo, G. G. Gurzadyan, S. Mhaisalkar, J. L. Brédas and C. Soci, *J. Mater. Chem. C*, 2017, **5**, 2771–2780.
103 Y. Boeije, W. T. M. Van Gompel, Y. Zhang, P. Ghosh, S. J. Zelewski, A. Maufort, B. Roose, Z. Y. Ooi, R. Chowdhury, I. Devroey, S. Lenaers, A. Tew, L. Dai, K. Dey, H. Salway, R. H. Friend, H. Sirringhaus, L. Lutsen, D. Vanderzande, A. Rao and S. D. Stranks, *J. Am. Chem. Soc.*, 2023, **145**, 21330–21343.
104 Y. Tian, Y. Li, B. Chen, R. Lai, S. He, X. Luo, Y. Han, Y. Wei and K. Wu, *J. Phys. Chem. Lett.*, 2020, **11**, 2247–2255.
105 A. H. Proppe, M. H. Elkins, O. Voznyy, R. D. Pensack, F. Zapata, L. V. Besteiro, L. N. Quan, R. Quintero-Bermudez, P. Todorovic, S. O. Kelley, A. O. Govorov, S. K. Gray, I. Infante, E. H. Sargent and G. D. Scholes, *J. Phys. Chem. Lett.*, 2019, **10**, 419–426.
106 A. Fakharuddin, M. Franckevičius, A. Devižis, A. Gelžinis, J. Chmeliov, P. Heremans and V. Gulbinas, *Adv. Funct. Mater.*, 2021, **31**, 2010076.
107 C. Wang, J. Si, L. Yan, T. Li and X. Hou, *J. Chem. Phys.*, 2024, **160**, 034704.
108 G. Gao, Y. Dong, L. Jiang, Q. Liu, X. Liu, Q. Chen, T. Wang and T. Zhu, *Nano Lett.*, 2024, **24**, 13356–13363.
109 J. Sun, X. Zhang, X. Ling, Y. Yang, Y. Wang, J. Guo, S. Liu, J. Yuan and W. Ma, *J. Mater. Chem. A*, 2021, **9**, 23019–23027.

110 Y. Jiang, M. Cui, S. Li, C. Sun, Y. Huang, J. Wei, L. Zhang, M. Lv, C. Qin, Y. Liu and M. Yuan, *Nat. Commun.*, 2021, **12**, 336.
111 L. Kong, X. Zhang, Y. Li, H. Wang, Y. Jiang, S. Wang, M. You, C. Zhang, T. Zhang, S. V. Kershaw, W. Zheng, Y. Yang, Q. Lin, M. Yuan, A. L. Rogach and X. Yang, *Nat. Commun.*, 2021, **12**, 1246.
112 X. Zang, S. Xiong, S. Jiang, D. Li, H. Wu, H. Ren, A. Cao, B. Li, Z. Ma, J. Chen, L. Ding, J. Tang, Z. Sun, J. Chu and Q. Bao, *Adv. Mater.*, 2024, **36**, 2309991.
113 L. Li, Y. Lai, H. Rao, W. Cai, X. Zhong, H. Guo and Z. Pan, *ChemSusChem*, 2025, e202402549.
114 J. Jiang, C. Tian, Z. Zhang, X. X. Liu, X. Wang, Y. Zheng, Z. Zhang, L. Wang, X. Wu, J. Liang and C. C. Chen, *Mater. Adv.*, 2022, **3**, 5786–5795.
115 K. Ma, J. Sun, H. R. Atapattu, B. W. Larson, H. Yang, D. Sun, K. Chen, K. Wang, Y. Lee, Y. Tang, A. Bhoopalam, L. Huang, K. R. Graham, J. Mei and L. Dou, *Sci. Adv.*, 2023, **9**, eadg0032.
116 M. D. Smith, A. Jaffe, E. R. Dohner, A. M. Lindenberg and H. I. Karunadasa, *Chem. Sci.*, 2017, **8**, 4497–4504.
117 Z. Zheng, S. Wang, Y. Hu, Y. Rong, A. Mei and H. Han, *Chem. Sci.*, 2022, **13**, 2167–2183.
118 Y. Gao, Z. Song, Q. Fu, Y. Chen, L. Yang, Z. Hu, Y. Chen and Y. Liu, *Adv. Mater.*, 2024, **36**, 2405921.
119 M. M. Davy, T. M. Jadel, C. Qin, B. Luyun and G. Mina, *Sustainable Energy Fuels*, 2021, **5**, 34–51.
120 H. Cao, T. Li, L. Zhao, Y. Qiang, X. Zheng, S. Dai, Y. Chen, Y. Zhu, L. Zhao, R. Cai, Z. Sun, F. Li, Y. Yang, L. Zhang, H. L. Yip and Z. Yu, *ACS Energy Lett.*, 2025, **10**, 2017–2025.
121 N. Jiang, Z. Wang, Y. Zheng, Q. Guo, W. Niu, R. Zhang, F. Huang and D. Chen, *Nano Energy*, 2022, **97**, 107181.
122 H. Lin, J. Mao, M. Qin, Z. Song, W. Yin, X. Lu and W. C. H. Choy, *Nanoscale*, 2019, **11**, 16907–16918.
123 Q. He, M. Worku, L. Xu, C. Zhou, H. Lin, A. J. Robb, K. Hanson, Y. Xin and B. Ma, *ACS Appl. Mater. Interfaces*, 2020, **12**, 1159–1168.
124 Y. Liu, S. Akin, A. Hinderhofer, F. T. Eickemeyer, H. Zhu, J. Y. Seo, J. Zhang, F. Schreiber, H. Zhang, S. M. Zakeeruddin, A. Hagfeldt, M. I. Dar and M. Grätzel, *Angew. Chem., Int. Ed.*, 2020, **59**, 15688–15694.
125 H. S. Kim, C. R. Lee, J. H. Im, K. B. Lee, T. Moehl, A. Marchioro, S. J. Moon, R. Humphry-Baker, J. H. Yum, J. E. Moser, M. Grätzel and N. G. Park, *Sci. Rep.*, 2012, **2**(1), 1–7.
126 K. Hisatsune, S. Uchida, T. N. Murakami and A. Kogo, *ACS Appl. Energy Mater.*, 2024, **7**, 5315–5320.
127 B. Chaudhary, T. M. Koh, B. Febriansyah, A. Bruno, N. Mathews, S. G. Mhaisalkar and C. Soci, *Sci. Rep.*, 2020, **10**(1), 1–11.
128 G. Yang, H. Gu, J. Yin, C. Fei, Z. Shi, X. Shi, X. Ying and J. Huang, *Nat. Sustainability*, 2025, **8**(4), 456–463.
129 P. Srivastava, S. Maity and V. Srinivasan, *J. Phys. Chem. C*, 2025, **129**, 1386–1397.
130 P. Srivastava, S. Maity and V. Srinivasan, *Small*, 2025, **21**, 2404493.
131 C. Liu, Z. Fang, J. Sun, Q. Lou, J. Ge, X. Chen, E. Zhou, M. H. Shang, W. Yang and Z. Ge, *ACS Energy Lett.*, 2020, **5**, 3617–3627.
132 J. Sun, Z. Ren, Z. Wang, H. Wang, D. Wu, X. W. Sun, W. C. H. Choy and K. Wang, *Adv. Opt. Mater.*, 2023, **11**, 2202721.
133 J. He, W. Sheng, J. Yang, Y. Zhong, Q. Cai, Y. Liu, Z. Guo, L. Tan and Y. Chen, *Angew Chem. Int. Ed. Engl.*, 2024, **63**, e202315233.
134 Q. Yao, Q. Xue, Z. Li, K. Zhang, T. Zhang, N. Li, S. Yang, C. J. Brabec, H. L. Yip and Y. Cao, *Adv. Mater.*, 2020, **32**, 2000571.
135 S. Ahmad, P. Fu, S. Yu, Q. Yang, X. Liu, X. Wang, X. Wang, X. Guo and C. Li, *Joule*, 2019, **3**, 794–806.
136 L. Lin, T. W. Jones, T. C. J. Yang, X. Li, C. Wu, Z. Xiao, H. Li, J. Li, J. Qian, L. Lin, J. Q. Shi, S. D. Stranks, G. J. Wilson and X. Wang, *Matter*, 2024, **7**, 38–58.
137 J. Rodríguez-Romero, J. Sanchez-Diaz, C. Echeverría-Arrondo, S. Masi, D. Esparza, E. M. Barea and I. Mora-Seró, *ACS Energy Lett.*, 2020, **5**, 1013–1021.
138 D. Zhang, C. Liu, J. Sun, Q. Xiong, X. Xiao, D. Li, B. Lyu, H. Su and W. C. H. Choy, *ACS Energy Lett.*, 2024, **9**, 1133–1140.
139 B. Zhao, Y. Lian, L. Cui, G. Divitini, G. Kusch, E. Ruggeri, F. Auras, W. Li, D. Yang, B. Zhu, R. A. Oliver, J. L. MacManus-Driscoll, S. D. Stranks, D. Di and R. H. Friend, *Nat. Electron.*, 2020, **3**(11), 704–710.
140 T. Niu, J. Lu, X. Jia, Z. Xu, M. C. Tang, D. Barrit, N. Yuan, J. Ding, X. Zhang, Y. Fan, T. Luo, Y. Zhang, D. M. Smilgies, Z. Liu, A. Amassian, S. Jin, K. Zhao and S. Liu, *Nano Lett.*, 2019, **19**, 7181–7190.
141 A. Forde, S. Tretiak and A. J. Neukirch, *Nano Lett.*, 2023, **23**, 11586–11592.
142 B. Liu, M. Long, M. Cai, L. Ding and J. Yang, *Nano Energy*, 2019, **59**, 715–720.
143 G. Li, J. Song, J. Wu, Z. Song, X. Wang, W. Sun, L. Fan, J. Lin, M. Huang, Z. Lan and P. Gao, *ACS Energy Lett.*, 2021, **6**, 3614–3623.
144 M. Bhatt, P. K. Nayak and D. Ghosh, *ACS Nano*, 2024, **18**, 24484–24494.
145 P. Chen, D. He, X. Huang, C. Zhang and L. Wang, *ACS Nano*, 2024, **18**(1), 67–88.
146 Z. Yang, J. Lai, R. Zhu, J. Tan, Y. Luo and S. Ye, *J. Phys. Chem. C*, 2022, **126**, 12689–12695.
147 R. Shi, R. Long, W. H. Fang and O. V. Prezhdo, *J. Am. Chem. Soc.*, 2023, **145**, 5297–5309.
148 J. He, W. H. Fang and R. Long, *J. Phys. Chem. Lett.*, 2020, **11**, 5100–5107.
149 Z. Guan, Y. Li, P. Man, H. Tan, Q. Wei, J. Liu, M. Li, T. H. Ly, J. Yin and C. S. Lee, *Adv. Mater.*, 2024, **36**, 2407406.
150 J. Hu, I. W. H. Oswald, S. J. Stuard, M. M. Nahid, N. Zhou, O. F. Williams, Z. Guo, L. Yan, H. Hu, Z. Chen, X. Xiao, Y. Lin, Z. Yang, J. Huang, A. M. Moran, H. Ade, J. R. Neilson and W. You, *Nat. Commun.*, 2019, **10**(1), 1–11.
151 R. Cao, K. Sun, C. Liu, Y. Mao, W. Guo, P. Ouyang, Y. Meng, R. Tian, L. Xie, X. Lü and Z. Ge, *Nano-Micro Lett.*, 2024, **16**, 1–16.

152 A. Musiienko, J. Pipek, P. Praus, M. Brynza, E. Belas, B. Dryzhakov, M. H. Du, M. Ahmadi and R. Grill, *Sci. Adv.*, 2020, **6**, 6393–6404.
153 Q. Sun, C. Zhao, Z. Yin, S. Wang, J. Leng, W. Tian and S. Jin, *J. Am. Chem. Soc.*, 2021, **143**, 19128–19136.
154 X. Chen, P. V. Kamat, C. Janáky and G. F. Samu, *ACS Energy Lett.*, 2024, **9**, 3187–3203.
155 L. Nienhaus, J. P. Correa-Baena, S. Wieghold, M. Einzinger, T. A. Lin, K. E. Shulenberger, N. D. Klein, M. Wu, V. Bulović, T. Buonassisi, M. A. Baldo and M. G. Bawendi, *ACS Energy Lett.*, 2019, **4**, 888–895.
156 S. Wieghold, A. S. Bieber, Z. A. VanOrman, L. Daley, M. Leger, J. P. Correa-Baena and L. Nienhaus, *Matter*, 2019, **1**, 705–719.
157 S. F. Zhang, X. K. Chen, A. M. Ren, H. Li and J. L. Bredas, *ACS Energy Lett.*, 2019, **4**, 17–25.
158 A. J. Magdaleno, M. Seitz, M. Frising, A. Herranz De La Cruz, A. I. Fernández-Domínguez and F. Prins, *Mater. Horiz.*, 2021, **8**, 639–644.